J Mater Sci (2023) 58:420–442

Metals & corrosion

Comparative evaluation of TiC and/or WC addition on microstructure, mechanical properties, thermal residual stress and reciprocating wear behaviour of ZrB_2–20SiC composites

Pradyut Sengupta[1,2], Suddhasatwa Basu[2,3], and Indranil Manna[1,4,*]

[1] Department of Metallurgical and Materials Engineering, Indian Institute of Technology Kharagpur, Kharagpur 721302, India
[2] CSIR–Institute of Minerals and Materials Technology, Bhubaneswar 751013, India
[3] Department of Chemical Engineering, Indian Institute of Technology Delhi, New Delhi 110016, India
[4] Birla Institute of Technology (BIT), Mesra, Ranchi 835215, India

Received: 16 August 2022
Accepted: 26 November 2022
Published online: 1 January 2023

ABSTRACT

The present study aims to evaluate and compare the effect of 5 vol.% TiC or WC addition on densification, phase stability, microstructure, mechanical properties, thermal residual stress and reciprocating wear behaviour of spark plasma-sintered ZrB_2-20 vol.% SiC composite. ZrB_2–20SiC–5TiC (vol.%) composite attains 99.6% mean sintered density even at 1700 °C, while WC containing composites (ZrB_2–20SiC–2.5TiC–2.5WC and ZrB_2–20SiC–5WC, vol.%) necessitates a sintering temperature of 1800 °C for > 98% densification. Phase and microstructure analyses confirm that respective incorporation of TiC and WC leads to in situ formation of $(Zr,Ti)B_2$ and $(Zr,W)B_2$ solid solution in the sintered composite. Elastic modulus and thermal expansion coefficients of the composites have been estimated utilizing well-established analytical models. The thermal residual stress of the sintered composites is determined analytically utilizing Taya's model and Hsueh's model and compared with residual stress of SiC reinforcement determined by Raman spectroscopy. Nano-indentation analysis confirms that the minimum resistance to deformation and maximum plasticity index are observed in ZrB_2–20SiC–2.5TiC–2.5WC composite due to its relatively low elastic modulus. The maximum Vickers hardness is observed in ZrB_2–20SiC–2.5TiC–2.5WC composite, whereas an excellent combination of indentation toughness and indentation modulus is found in ZrB_2–20SiC–5WC. Owing to relatively high fracture toughness exponent and low brittleness index, ZrB_2–20SiC–5WC composite records the minimum wear volume and wear rate in linear reciprocating wear test.

Handling Editor: Megumi Kawasaki.

Address correspondence to E-mail: imanna@metal.iitkgp.ernet.in; imanna@bitmesra.ac.in
E-mail Addresses: pradyuts@iitkgp.ac.in; pradyut@immt.res.in; sbasu@immt.res.in; sbasu@iitd.ac.in

https://doi.org/10.1007/s10853-022-08021-x

GRAPHICAL ABSTRACT

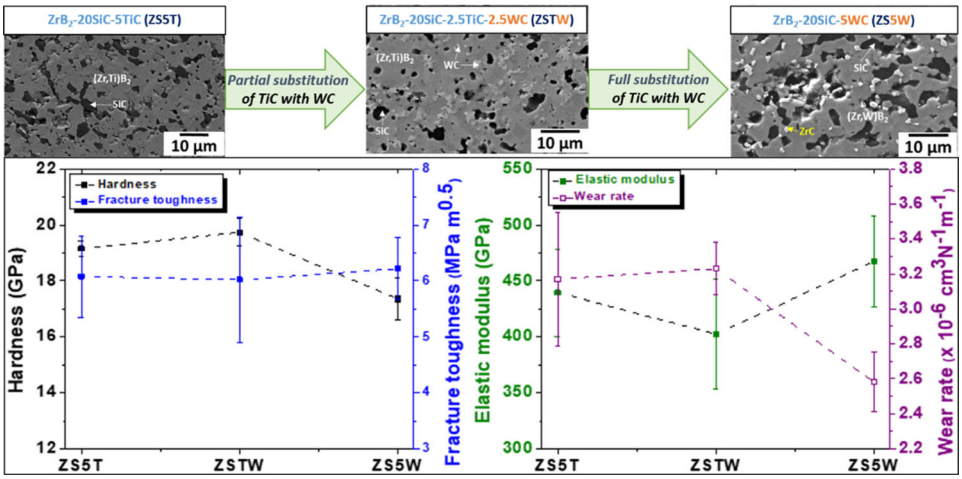

Introduction

In order to realize the human ambition to explore and inhabit the outer space in the future, many research groups evince continued research interest to design and develop thermal protection system for next-generation hypersonic space vehicles [1, 2]. Owing to extremely high melting point (> 3000 °C) and most attractive mechanical properties as well as oxidation resistance at very high temperature (> 1500 °C), ultra-high-temperature ceramics (UHTC)—a special class of advanced materials, are being explored as structural material for critical applications [3]. ZrB_2-, HfB_2-, TiB_2-, ZrC-, HfC-based UHTCs are developed either as independent structural components or as an additive to C/C composites [3–5]. Amongst the possible candidates for development of UHTCs, ZrB_2–SiC system has received considerable and consistent attention of various research groups across the world [3, 6–8]. Due to strong covalent bonding and extremely sluggish self-diffusion coefficient, the conventional sintering of ZrB_2 or its composites necessitate very high sintering temperature (2150 °C) for prolonged duration (9 h), which invariably leads to excessive grain growth and poor hardness (14.5 ± 2.6 GPa) [9]. To circumvent this hurdle, pressure assisted densification routes like spark plasma sintering (SPS [10]) or hot pressing (HP [11]) have been adopted by several researchers for fabricating dense ZrB_2-based composites with a shorter sintering cycle. However, relatively poor fracture toughness [12] of ZrB_2-based ceramic matrix composites is a matter of concern for high-temperature structural applications in hypersonic space vehicles. In order to improve sinterability, fracture toughness, oxidation and/or ablation resistance, many research groups have made extensive efforts to assess the role of metallic [13], oxide [14], carbide [15], nitride [16], silicide [17] and carbon-based additives [18] on ZrB_2 or ZrB_2–SiC UHTC composites.

Lately, the present authors have demonstrated the merit of Al alloy sinter additive on densification and mechanical properties of ZrB_2–SiC composite [13]. Amongst various additives, the role of WC on densification, microstructure, mechanical and oxidation behaviour of these composites has received significant research attention globally in the past few years [19–21]. Monteverde and Silvestroni [19] evaluated the combined effect of WC and SiC reinforcement in ZrB_2 and reported high temperature flexural strength of the composites. The ambient temperature flexural strength of ZrB_2-15WC (vol.%) and ZrB_2–15SiC–5WC (vol.%) composites was 631 ± 106 MPa and 543 ± 41 MPa, which decreased to 596 ± 53 MPa and 426 ± 15 MPa at 1500 °C, respectively. The

retention of high temperature strength in ZrB_2-15WC and ZrB_2–15SiC–5WC composites was attributed to the combined effect of evolution of core–shell structure and formation of $(Zr,W)B_2$ solid solution. In hot pressed ZrB_2-20SiC-5WC (vol.%) composite, flexural strength of 675 ± 33 MPa was reported by Zou et al. [20] Lately, Silvestroni et al. [22] developed super-strong ZrB_2-3 vol.% SiC-5 vol.%WC composite by hot pressing and observed the formation of $(Zr,W)B_2$ shell surrounding ZrB_2 core. The same study reported unusually high flexural strength (836 ± 103 MPa) at 1800 °C due to grain refinement and formation of core–shell structure.

In a recent study [23], the present authors have demonstrated that 5–10 vol.% of TiC addition improves densification, hardness, fracture toughness and flexural strength of ZrB_2–20SiC (vol.%) composites and reduces the sintering temperature by 200 °C. In this context, it is worth noting that both TiC and WC exhibit high melting point ($(T_m)_{TiC}$ = 3067 °C, $(T_m)_{WC}$ = 2870 °C), excellent combination of hardness ($(H)_{TiC}$ = 28–35 GPa, $(H)_{WC}$ = 18–22 GPa) and elastic modulus ($(E)_{TiC}$ = 410–510 GPa, $(E)_{WC}$ = 600 GPa) [24, 25]. Despite resemblance in terms of mechanical behaviour, there is no comparative analysis to examine the relative efficacy of TiC vis-à-vis WC addition on structure–property correlation of ZrB_2–SiC composite. Furthermore, the utility of combined addition of both WC and TiC in ZrB_2–SiC system has not been explored. Thus, a detailed assessment of the suitability of TiC and/or WC as a reinforcement material in ZrB_2–SiC composite is now warranted.

During launch or re-entry, the space vehicle may experience collision with small but sharp particles or debris, which can lead to abrasive or erosive wear of the surface of the thermal protection system [26]. Therefore, it is extremely important to assess the wear behaviour of the UHTC composites. Even though the mechanical properties, thermal shock resistance, oxidation and ablation behaviour of UHTC composites have been explored by different research groups [27, 28], relatively less attention has been devoted towards tribological analysis of these composites. Since this study evaluates the relative effectiveness of TiC and WC as a prospective reinforcement in ZrB_2–SiC composite, it is also desirable that the wear behaviour of these composites is evaluated in addition to assessing microstructure, hardness, elastic modulus and fracture toughness.

Therefore, the overall objective of the present study is to evaluate the role of TiC and WC addition (independently or in combination) on phase and microstructure evolution, and measurement of hardness, fracture toughness, elastic modulus, thermal expansion coefficient and thermal residual stress ZrB_2-based composites consolidated by spark plasma sintering. This will be the first report on comparative evaluation of the effect of TiC and WC addition (independently and in combination) on structure–property relationship of ZrB_2–20 vol.% SiC composites.

Materials and methods

Fabrication of composites

In order to develop UHTC composites, high-purity ZrB_2, SiC, TiC and WC powders, as listed in Table 1, were used as starting materials for the synthesis of the composites.

In order to examine the relative effectiveness of TiC and WC addition on densification and relevant mechanical properties, three different compositions were chosen, namely, ZrB_2–20 vol.% SiC–5 vol.% TiC (the base composite, hereinafter referred to as ZS5T), ZrB_2–20 vol.% SiC–2.5 vol.% TiC–2.5 vol.% WC (hereinafter referred to as ZSTW) and ZrB_2–20 vol.% SiC–5 vol.% WC (hereinafter referred to as ZS5W). Based on the compositions selected, the constituents were mixed in the appropriate proportion in a mortar–pestle for 30 min, followed by ball milling for 2 h in high-energy planetary ball mill (Insmart) with 300 revolution per minute (rpm) speed and 10:1 ball to powder weight ratio using WC coated steel vials. In order to avoid oxidation and ensure homogeneous grinding and mixing, analytical grade toluene was used as process control agent. Furthermore, the ball milling operation was stopped for 15 min after every 30 min of operation for avoiding excessive heating. Table 2 summarizes the composition, nomenclature, theoretical density (computed using the inverse rule of mixture) and crystallite size (determined from separate diffraction peak broadening analysis) of ZrB_2, SiC, TiC and WC in the milled powders.

Table 1 The manufacturer, purity, density, particle size and lattice parameter of the as-received powders used in this work

Material	Manufacturer	Purity (%)	Density (g cm^{-3})	Particle size (μm)	Lattice parameter (nm)
ZrB_2 (Grade B)	H.C Starck, Germany	> 99	6.10	1.5–3.0	$a = b = 0.316 \pm 0.000$, $c = 0.353 \pm 0.000$
SiC	Nanoshel, UK	> 99	3.21	< 2	$a = b = 0.309$, $c = 1.517$
TiC	Nanoshel, UK	> 99	4.91	< 2	$a = b = c = 0.432$
WC	Nanoshel, UK	> 99	15.63	< 2	$a = b = 0.290$, $c = 0.283$

Table 2 The composition, nomenclature, theoretical density and crystallite size of different phases in milled powders

Composition (vol.%)	Nomenclature	Theoretical density (g cm^{-3})	Crystallite size (nm) of milled powder			
			ZrB_2	SiC	TiC	WC
ZrB_2–20SiC–5TiC	ZS5T	5.46	46 ± 4	22 ± 6	22 ± 8	–
ZrB_2–20SiC–2.5TiC–2.5WC	ZSTW	5.73	51 ± 3	28 ± 5	25 ± 6	30 ± 7
ZrB_2–20SiC–5WC	ZS5W	6.00	49 ± 5	31 ± 7	–	31 ± 6

Phase and microstructural analyses

Following the phase analysis by X-ray diffraction (XRD) (Panalytical X'Pert Pro using Cu-K_α radiation with wavelength, λ_{Cu} =0.154 nm), hot consolidation of the composites into discs of 20 mm diameter and 6 mm height was carried out by spark plasma sintering (SPS) (Dr. Sinter SPS system) at 1700 and 1800 °C for 10 min in Ar atmosphere under 70 MPa pressure. After SPS, the adherent graphite layers were removed from the sintered composites by shallow hand grinding. Subsequently, the sintered density or relative density (expressed as per cent of theoretical density) of the composites was estimated using Archimedes principle with distilled water as the immersion medium. The microstructure of the polished sections of the composites was examined by scanning electron microscopy (SEM) (using a Zeiss, EVO18 machine) equipped with energy dispersive spectroscopy (EDS) facility (EDAX, AMETEK, USA). Microstructural study at higher resolution and phase identification of specific regions was conducted by transmission electron microscopy (TEM) (using FEI, Tecnai G2 20) of the composite powders obtained by grinding the sintered samples in a mortar–pestle for 4 h and collecting the finest ones by fishing and drop casting on carbon coated Cu grid following ultrasonication for 30 min in ethanol medium. TEM analysis was possible only along the electron transparent edges of some of these randomly dispersed particles collected on the Cu grid after proper drying.

Evaluation of mechanical properties, thermal residual stress and wear behaviour

The hardness of the sintered UHTC composites was measured using a Vickers hardness tester (Matsuzawa, Japan). The applied load (P) and dwell time were 100 gf and 10 s, respectively. The Vickers hardness (H) of the composites was analytically estimated using the following relation:

$$H = 1.854\left(\frac{P}{d^2}\right). \quad (1)$$

In Eq. (1), $d = \left(\frac{d_1+d_2}{2}\right)$, where d_1 and d_2 stand for the diagonals of the indentation mark on the sample.

In order to determine the indentation toughness (K_c) of the UHTC composites, the composites were subjected to 10 kgf load for 10 s in Vickers hardness tester (FIE, India). The diagonal crack length (d) was estimated from SEM images of the indentation mark using ImageJ software and fed into the widely used Anstis equation [29], as stated below:

$$K_c = 0.016\left(\frac{E}{H}\right)^{1/2}\left(\frac{P}{c^{3/2}}\right) \quad (2)$$

where E and H are the elastic modulus and hardness of the sample, respectively. At least 10 readings were recorded on each sample to obtain the mean and standard deviation of the indentation toughness. For determination of indentation toughness, the applied load and dwell time were 10 kgf and 10 s, respectively. In this work, the elastic moduli of the composites were

estimated both analytically and experimentally (using nano-indentation). The modulus value obtained by nano-indentation technique was utilized in determination of indentation toughness (as reported in earlier studies [30, 31]). The Poisson's ratio (v) of ZS5T, ZSTW and ZS5W composites were estimated using rule of mixture considering v of ZrB_2, SiC, TiC and WC as 0.144, 0.14, 0.187 and 0.24, respectively [32, 33]. The critical energy release rate (G_c) was determined using the following equation:

$$G_c = K_c^2\left(\frac{1-v^2}{E}\right). \quad (3)$$

The nano-mechanical behaviour of the spark plasma-sintered UHTC composites was evaluated using instrumented nano-indentation system (Anton Paar) following Oliver–Pharr method [34]. For determining nano-hardness, elastic modulus, maximum penetration depth, final depth and stiffness, at least 16 readings were recorded on each composite. In all cases, the maximum applied load was 450 mN and the dwell time was 10 s at the maximum load.

Coefficient of thermal expansion and thermal residual stress of sintered ZS5T, ZSTW and ZS5W UHTC composites were evaluated using various well-established analytical models. The residual compressive stress of SiC grains has been determined using Raman spectroscopy (Renishaw inVia micro-Raman Spectrometer) using a 532 nm laser radiation. The linear reciprocating wear behaviour of the well-polished sections of the composites was assessed in ambient condition using a ball-on-plate type wear tester (Rtec) fitted with a 6 mm diameter sintered WC-Co ball (used as a counter body) under 10 N compressive load, applied for 10 min dwell time at a frequency of 10 Hz. The stroke length was 2 mm in all cases. At least three readings were recorded on each composite under identical condition. The wear track profile was recorded by optical profilometry in addition to SEM–EDS analysis of the wear tracks for relative assessment of damage induced by wear studies.

Results and discussion

Effect of TiC and/WC addition on densification

In a recent study [23], the present authors have demonstrated that addition of TiC in ZrB_2–SiC significantly enhances sinterability due to which, the maximum sintered density of ZrB_2–20SiC–5TiC (vol.%) and ZrB_2–20SiC–10TiC (vol.%) composites consolidated by SPS at 1700 °C for 5 min could reach up to 99.6% (theoretical). In order to investigate the relative merit of WC and TiC addition, three different composites, namely, ZS5T, ZSTW and ZS5W were sintered at 1700 °C by SPS. It was found that the respective mean relative density of ZSTW and ZS5W could reach only up to 95.1% and 93.2% indicating that WC containing composites would require relatively higher sintering temperature for full densification. Earlier, Zou et al. [20] obtained a relative density of 99% in ZrB_2–20SiC–5WC composite only by hot pressing at 1900 °C for 30 min under 60 MPa. In order to realize greater densification, the ZS5T, ZSTW and ZS5W composites were sintered by SPS at higher temperature (= 1800 °C) for 10 min under 70 MPa pressure which yielded sintered density of 98.33 ± 0.47 and 99.65 ± 0.30% (theoretical) for ZSTW and ZS5W, respectively. Interestingly, TiC containing ZS5T achieved complete densification at 1800 °C. Thus, it was decided that the present set of UHTCs, (ZS5T, ZSTW and ZS5W) would be consolidated by SPS only at 1800 °C to obtain adequate densification needed for meaningful investigation and comparison of mechanical properties of interest.

Phase analyses of milled and sintered composites

Figure 1 exhibits the XRD patterns of high-energy ball milled ZS5T, ZSTW and ZS5W composite powders. The presence of the respective constituent phases, i.e. ZrB_2, SiC, TiC (in ZS5T), ZrB_2, SiC, TiC, WC (in ZSTW), and ZrB_2, SiC, WC (in ZS5W) is evident in milled powders. Due to higher volume fraction (75 vol.%), the most intense peak corresponds to ZrB_2 in all powders. The crystallite size of ZrB_2, SiC, TiC and WC phases in the milled ZS5T, ZSTW and ZS5W powders has been calculated using Scherrer formula [35] and is shown in Table 2.

The phase analysis of spark plasma-sintered composites is presented in Fig. 2. Contrary to the phase analysis of milled ZS5T, no trace of TiC has been observed in the XRD pattern of sintered ZS5T, suggesting that TiC has possibly reacted with ZrB_2 during the SPS process to yield $(Zr,Ti)B_2$ solid solution. The detail explanation of the evolution of in situ $(Zr,Ti)B_2$ solid solution in ZrB_2–SiC–TiC can be found

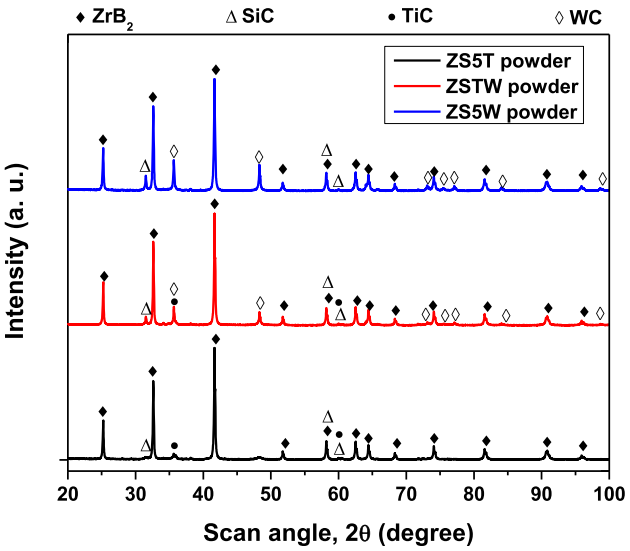

Figure 1 X-ray diffraction patterns of ball milled ZS5T, ZSTW and ZS5W powders exhibit the presence of individual phases. In all samples, the most intense peak corresponds to ZrB_2.

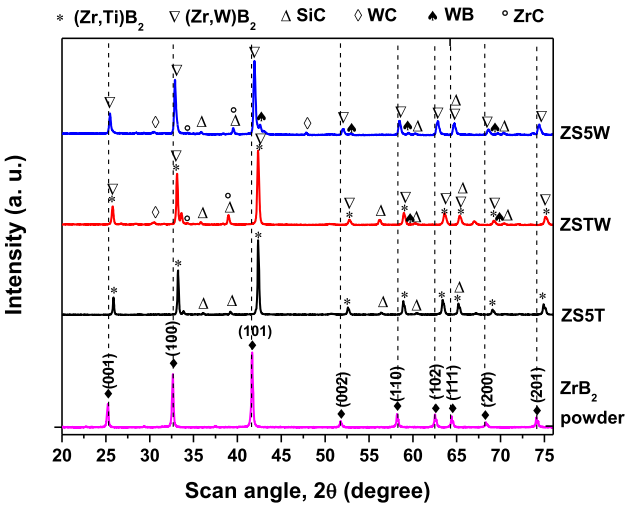

Figure 2 X-ray diffraction patterns of spark plasma-sintered ZS5T, ZSTW and ZS5W composites. For comparison, the reference pattern of ZrB_2 powder is also shown.

in our recent study [23]. Previous studies on ZrB_2–SiC–WC composite revealed the formation of core-rim substructure, where ZrB_2 core is encapsulated by $(Zr,W)B_2$ rim [19, 22]. Moreover, the XRD patterns of ZS5W and ZSTW indicate the presence of ZrC and WB, formed as in situ reaction product during SPS of ZrB_2–SiC–TiC–WC and ZrB_2–SiC–WC composite systems. In contrast, similar reaction products (ZrC, TiB, TiB_2, etc.) are not found in XRD analysis of sintered ZS5T composite. The phase analyses of sintered ZSTW and ZS5W composites also reveal the presence of free or unreacted WC, whereas no TiC has been detected in the XRD pattern of ZS5T composite.

For the convenience of comparison, the XRD pattern of ZrB_2 (PDF no. 34-0423) is also included in Fig. 2. It is evident that peaks corresponding to ZrB_2 or its solid solution have shifted towards higher scanning angle (2θ) value in sintered ZS5T, ZSTW and ZS5W composites. For example, the most intense (101) peak of pure ZrB_2 that usually occurs at $2\theta = 41.63°$ is located in Fig. 2 for the sintered ZS5T, ZSTW and ZS5W composites at $2\theta = 42.38°$, 42.35° and 42.58°, respectively. The slight peak shift towards higher scan angle implies that the corresponding lattice parameters of the concerned phases must have systematically decreased owing to dissolution of TiC and/or WC in ZrB_2 as a solid solution. From the XRD patterns of sintered composites, the lattice parameters of hexagonal solid solution phase are determined and presented in Table 3. In accordance with the peak shift towards higher scan angle, both lattice parameters (a and c) of hexagonal solid solution phase in ZS5T ($a = b = 0.314 \pm 0.000$ nm, $c = 0.348 \pm 0.002$ nm), ZSTW ($a = b = 0.313 \pm 0.001$ nm, $c = 0.347 \pm 0.001$ nm) and ZS5W ($a = b = 0.314 \pm 0.001$ nm, $c = 0.347 \pm 0.002$ nm) are found to be slightly lower than that of pure ZrB_2 powder ($a = b = 0.316 \pm 0.000$ nm, $c = 0.353 \pm 0.000$ nm, $c/a = 1.115 \pm 0.001$) used as a starting material. Compared to ZrB_2, the c/a ratio of the hexagonal solid solution phase in ZS5T was slightly lower (1.110). With incorporation of 2.5 and 5 vol.% WC, the c/a ratio of the resultant solid solution was further decreased to 1.108 and 1.105 in ZSTW and ZS5W, respectively. It may be pointed out that Fahrenholtz et al. [6] predicted that formation of $(Zr,M)B_2$ (where M = Ti, Nb and similar early transition metals) in ZrB_2-based UHTC system would primarily depend on diffusion of M atoms in Zr as strongly bonded interstitial B atoms are unlikely to migrate or play any major role in such $(Zr,Ti)B_2$ or $(Zr,Nb)B_2$ compound or solid solution formation. This conclusion implies that the formation of $(Zr,Ti)B_2$ solid solution in the sintered composites will primarily depend on the diffusion of Ti or Ti^{4+} in Zr (or ZrB_2). Similarly, the diffusion of W or W^{4+} in Zr or ZrB_2 gives rise to the in situ formation of $(Zr,W)B_2$ solid solution phase. In addition to the lattice parameters of hexagonal solid solution phase, the lattice parameters of WB and ZrC phases have been determined from XRD patterns of ZSTW and ZS5W and are reported in Table 3.

Table 3 Mean sintered density of the composites, crystallite size and lattice parameter of different phases

Composite	Mean sintered density (% theoretical)		Crystallite size (nm)		Lattice parameter (nm)		
	1700 °C	1800 °C	WB	ZrC	Hexagonal solid solution	WB	ZrC
ZS5T	99.60	100.0	–	–	$a = b = 0.314 \pm 0.000$, $c = 0.348 \pm 0.002$	–	–
ZSTW	95.10	98.33	31 ± 8	30 ± 6	$a = b = 0.313 \pm 0.001$, $c = 0.347 \pm 0.001$	$a = b = 0.309 \pm 0.004$, $c = 1.695 \pm 0.004$	$a = b = c = 0.468 \pm 0.003$
ZS5W	93.20	99.65	44 ± 8	34 ± 13	$a = b = 0.314 \pm 0.001$ $c = 0.347 \pm 0.002$	$a = b = 0.309 \pm 0.002$ $c = 1.690 \pm 0.003$	$a = b = c = 0.469 \pm 0.001$

The crystallite size and lattice parameter were determined from XRD patterns of composites sintered at 1800 °C

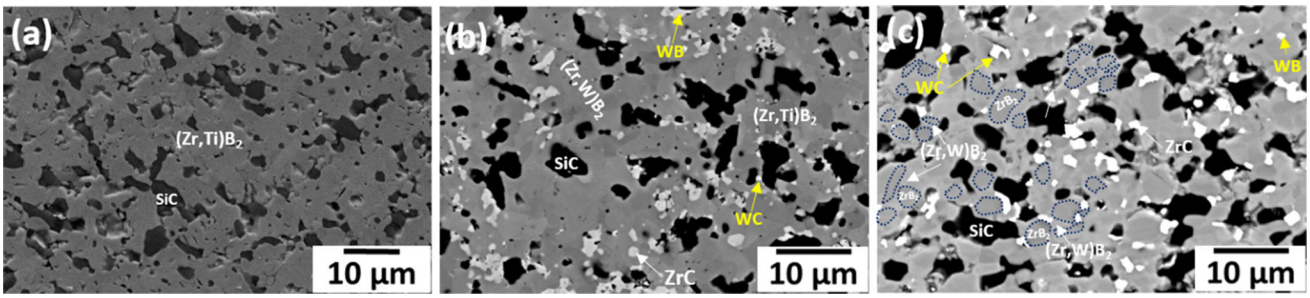

Figure 3 SEM images of **a** ZS5T, **b** ZSTW and **c** ZS5W composites sintered at 1800 °C.

Analysis of microstructure

Figure 3 presents the SEM images of ZS5T, ZSTW and ZS5W UHTC composites prepared by SPS at 1800 °C. EDS point analysis was conducted to determine local or micro-composition of a given phase for an approximate idea of its possible identity. Figure 3a shows the microstructure of ZS5T in secondary electron imaging mode, where SiC grains and $(Zr,Ti)B_2$ solid solution phases can be distinguished as dark grey faceted phases and light grey polyhedral grains, respectively. In accordance with the earlier measured density values, no porosity was detected in sintered ZS5T. Our previous work [23] on ZrB_2–SiC–TiC system also revealed that TiC addition leads to formation of $(Zr,Ti)B_2$ solid solution in spark plasma-sintered composite. Moreover, no unreacted or free TiC is noticed in Fig. 3a, which indicates that entire 5 vol.% TiC has been dissolved in ZrB_2 to yield $(Zr,Ti)B_2$ solid solution in sintered ZS5T composite. Indeed, the formation of $(Zr,Ti)B_2$ solid solution is plausible in TiC containing ZrB_2-SiC composite since Zr-Ti binary system is isomorphous in nature with unrestricted solid solubility in the entire compositional range [36]. Additionally, it is to be noted that, no other reaction product like ZrC, TiB or TiB_2 was observed in the SEM images of ZS5T.

Figure 3b, c shows the microstructures of ZSTW and ZS5W, respectively. Owing to the combined effect of TiC and WC, two different solid solutions, i.e. $(Zr,Ti)B_2$ and $(Zr,W)B_2$ were formed in ZSTW. On the other hand, the formation of core-rim structure, i.e. $(Zr,W)B_2$ rim surrounding ZrB_2 core was noticed in ZS5W (Fig. 3c). The core-rim structure is also shown using blue-dotted line in Fig. 3c, where the 'core' region (within the blue-dotted area) represents ZrB_2 and the 'rim' stands for $(Zr,W)B_2$ solid solution. It may be mentioned that the previous studies [19, 20] on ZrB_2-SiC-WC UHTC composites also reported the formation of core-rim structure, where ZrB_2 core was surrounded with a rim of $(Zr,W)B_2$. Interestingly, isolated presence of free or unreacted WC was noticed in sintered ZSTW and ZS5W, indicating that the entire amount of WC was not dissolved or reacted during sintering by SPS. In addition, ZrC and WB phases were found in WC containing composites, confirming the earlier observation from XRD analysis (Fig. 2) of the sintered composites. The distribution of SiC is found to be uniform in ZS5T, ZSTW and ZS5W composites.

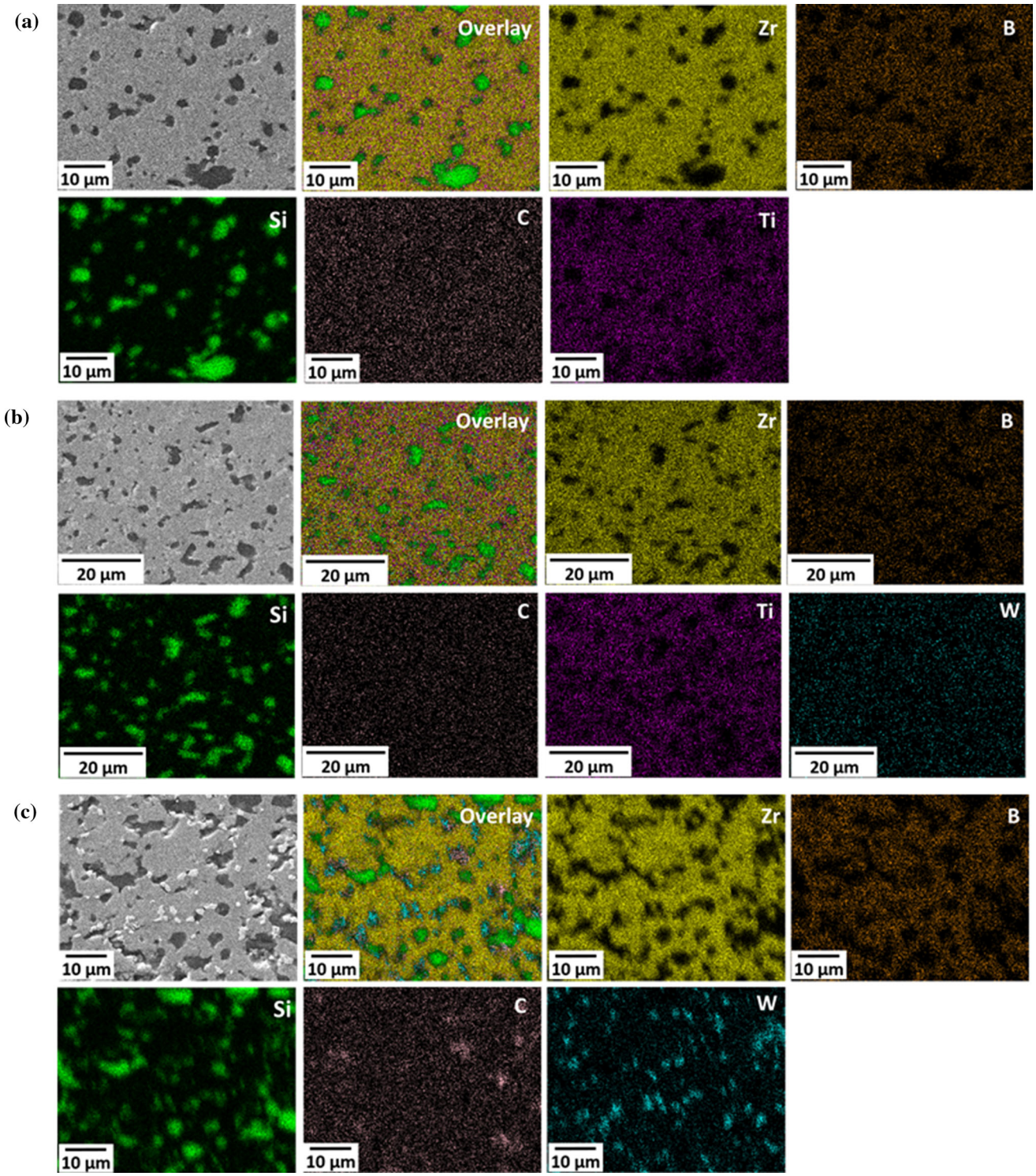

Figure 4 Elemental map showing the distribution of constituent elements in spark plasma-sintered **a** ZS5T, **b** ZSTW and **c** ZS5W composites.

The SEM–EDS elemental compositional maps of ZS5T, ZSTW and ZS5W composites are shown in Fig. 4a–c, respectively. In line with the XRD and SEM analyses, the formation of $(Zr,Ti)B_2$ solid solution was confirmed in ZS5T and ZSTW with the help of EDS mapping. In case of WC containing ZSTW and ZS5W

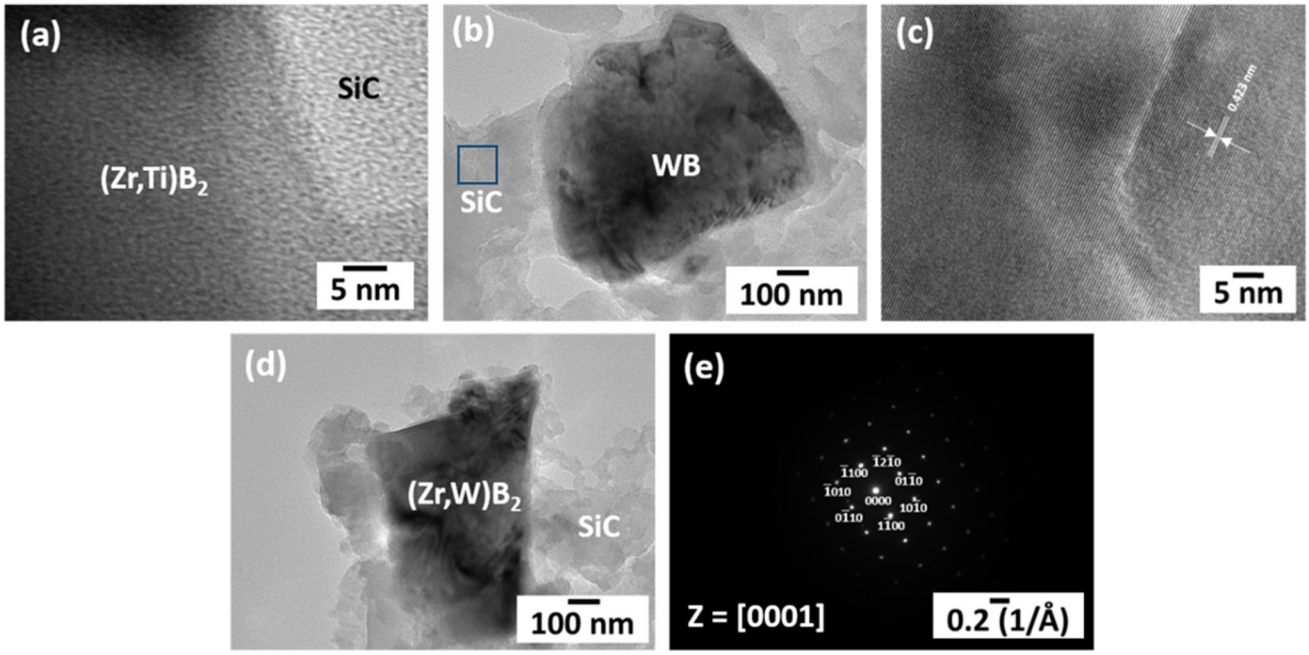

Figure 5 High resolution transmission electron micrographs of **a** ZS5T, **b**, **c** ZSTW and **d** ZS5W composites. The lattice fringes from (0004) plane of tetragonal WB are shown in **c**. The representative selected area diffraction pattern from [0001] zone axis of SiC (from the marked region of **b**) is shown in **e**.

composites, $(Zr,W)B_2$ solid solution formation is indicated. The reason behind $(Zr,Ti)B_2$, $(Zr,W)B_2$ solid solution formation and the presence of in situ phases like ZrC, WB is explained in "Thermodynamic analysis of possible reaction mechanisms and solid solution formation" section.

Figure 5 shows the representative TEM images of (a) ZS5T, (b-c) ZSTW and (d) ZS5W composites prepared by SPS at 1800 °C for 10 min. The presence of $(Zr,Ti)B_2$ and SiC is found in ZS5T (Fig. 5a). Previously, SEM–EDS analyses (Figs. 3a, 4a) of sintered ZS5T composite revealed the presence of two distinct phases, namely, $(Zr,Ti)B_2$ and SiC. In addition, no contamination due to WC could be detected in SEM–EDS analyses of ZS5T even though WC balls and jars were used for high-energy milling of ZrB_2, SiC and TiC powders. In corroboration with SEM analysis, TEM study confirms that WC impurity is absent in the sintered ZS5T composite. The representative bright field TEM image of ZSTW dictate the presence WB and SiC reinforcement, where the former has formed in situ during SPS. The high resolution lattice fringes from WB phase shows an interplanar spacing of 0.423 nm, which corresponds to (0004) plane of WB. The formation of $(Zr,W)B_2$ solid solution is observed in ZS5W (Fig. 5d). Figure 5e exhibits the SADP originated from [0001] zone axis of SiC. The SADP was captured from the marked region (blue square box) of Fig. 5b.

Thermodynamic analysis of possible reaction mechanisms and solid solution formation

In the present study, TiC and WC have either been added to ZrB_2–SiC separately (as in ZS5T and ZS5W) or together (as in ZSTW). Therefore, it is important to investigate the state or phase (unreacted, solid solution or reacted) of these compounds retained in ZS5T, ZSTW and ZS5W composites following the sintering by SPS at 1800 °C. Accordingly, thermodynamic feasibility of different chemical reactions has been analysed utilizing HSC Chemistry software (v. 9.9) in terms of the variation in Gibbs energy (ΔG) with reaction temperature, as shown in Fig. 6:

$$ZrB_2 + TiC = ZrC + TiB_2 \quad (4)$$

$$3TiC + ZrO_2 = ZrC + 3Ti + 2CO(g) \quad (5)$$

$$3WC + ZrO_2 = ZrC + 3W + 2CO(g) \quad (6)$$

$$3ZrB_2 + 6TiC + ZrO_2 = 4ZrC + 6TiB + 2CO(g) \quad (7)$$

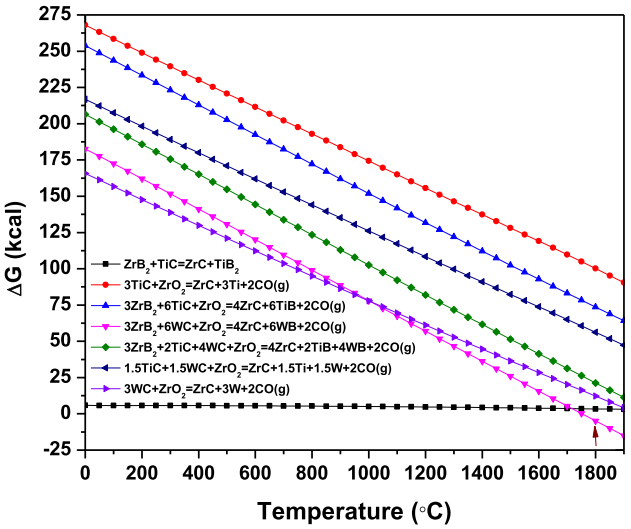

Figure 6 The change in Gibbs energy with temperature (calculated using HSC Chemistry software). The arrow indicates that only one reaction ($3ZrB_2 + 6WC + ZrO_2 = 4ZrC + 6WB + 2CO(g)$) is thermodynamically feasible (i.e. $\Delta G < 0$) in the spark plasma sintering temperature (1800 °C).

$$3ZrB_2 + 6WC + ZrO_2 = 4ZrC + 6WB + 2CO(g) \quad (8)$$

$$3ZrB_2 + 2TiC + 4WC + ZrO_2 = 4ZrC + 2TiB + 4WB + 2CO(g) \quad (9)$$

$$1.5TiC + 1.5WC + ZrO_2 = ZrC + 1.5Ti + 1.5W + 2CO(g). \quad (10)$$

It may be mentioned that HSC Chemistry software is also utilized by many published literature [13, 23, 37–39] on UHTC systems to determine thermodynamic feasibility of various chemical reactions or phase stability diagrams of ZrB_2-based UHTC systems.

For a ready reference, ΔG values of the above reactions at the SPS temperature (1800 °C) are summarized in Table 4. From Fig. 6 and Table 4, it is evident that ZrO_2 oxide scale, which is present as an impure phase surrounding ZrB_2 particles, does not get reduced by TiC and/or WC additions according to Eqs. (5) and (6), respectively. Hence, the possibility of obtaining metallic Ti (in ZS5T, ZSTW) and W (in ZS5W, ZSTW) in the sintered composite can be ruled out. Table 4 and Fig. 6 also suggest that only reaction (8) is thermodynamically feasible at the sintering temperature. Indeed, ZrC and WB phases were detected in SEM images of sintered ZS5W and ZSTW, where 5 and 2.5 vol.% of WC were added, respectively. Based on the thermodynamic analysis, it can be inferred that ZrC and WB are formed in situ as a reaction product when WC is present in the composite system (i.e. ZS5W and ZSTW). In other words, the formation of ZrC is not thermodynamically feasible in ZS5T where WC is absent.

In the literature, the formation of $(Zr,W)B_2$, $(Zr,Ti)B_2$, $(Zr,Mo)B_2$ shell or rim structure surrounding ZrB_2 grain has been reported in sintered ZrB_2-SiC composite as a consequence of the respective addition of WC [19], TiC [23] and $MoSi_2$ [40]. In line with the observations in these published literature, the presence of $(Zr,Ti)B_2$ and $(Zr,W)B_2$ solid solutions were detected in this study due to respective addition of TiC and WC in ZrB_2–SiC.

The atomic radii of Zr, Ti and W are 0.159, 0.145 and 0.137 nm, respectively [41]. Furthermore, the respective cationic (+ 4) radii of Zr, Ti and W are 0.079, 0.068 and 0.070 nm [41]. Hence, the radius ratios of $\frac{r_{Ti}}{r_{Zr}}$, $\frac{r_W}{r_{Zr}}$, $\frac{r_{Ti}^{4+}}{r_{Zr}^{4+}}$ and $\frac{r_W^{4+}}{r_{Zr}^{4+}}$ are found to be 0.91, 0.86, 0.86 and 0.89, respectively. These ratios indicate that the difference in atomic and ionic radii is < 15% in Ti–Zr, W–Zr, Ti^{4+}–Zr^{4+} and W^{4+}–Zr^{4+} pairs. As a result, the in situ formation of $(Zr,Ti)B_2$ and $(Zr,W)B_2$ solid solutions is thermodynamically feasible according to the size factor rule of Hume-Rothery [41] in TiC and WC containing ZrB_2–SiC composites, respectively. Since ZSTW contains both the carbides (TiC and WC) in equal volume fraction, the coexistence of $(Zr,Ti)B_2$ and $(Zr,W)B_2$ solid solutions is not unusual at all.

Effect of TiC and WC addition on hardness and fracture toughness

The measured Vickers hardness and calculated values of indentation toughness and critical energy release rate of sintered ZS5T, ZSTW and ZS5W composites are documented in Table 5, which suggests that TiC containing UHTC composites (ZS5T and ZSTW) exhibit better hardness compared to 5 vol.% WC containing ZS5W. While the minimum hardness of 17.49 ± 0.74 GPa was obtained in case of ZS5W, the maximum recorded hardness of ZSTW was 19.89 ± 0.65 GPa. The high hardness in TiC containing ZS5T and ZSTW can be attributed to solid solution strengthening due to formation of $(Zr,Ti)B_2$ and dispersion strengthening owing to the presence of uniformly distributed discrete SiC particles.

Table 4 The change in Gibbs energy (ΔG) at 1800 °C of various probable chemical reaction between constituent phases

Probable chemical reaction between the constituent phases	ΔG(kcal) at 1800 °C	Thermodynamic feasibility of the reaction at 1800 °C
$ZrB_2 + TiC = ZrC + TiB_2$	3.39	Not feasible
$3TiC + ZrO_2 = ZrC + 3Ti + 2CO(g)$	100.14	Not feasible
$3ZrB_2 + 6TiC + ZrO_2 = 4ZrC + 6TiB + 2CO(g)$	73.63	Not feasible
$3ZrB_2 + 6WC + ZrO_2 = 4ZrC + 6WB + 2CO(g)$	− 4.92	Feasible
$3ZrB_2 + 2TiC + 4WC + ZrO_2 = 4ZrC + 2TiB + 4WB + 2CO(g)$	21.26	Not feasible
$1.5TiC + 1.5WC + ZrO_2 = ZrC + 1.5Ti + 1.5W + 2CO(g)$	56.15	Not feasible
$3WC + ZrO_2 = ZrC + 3W + 2CO(g)$	12.17	Not feasible

Table 5 Summary of Vickers hardness, indentation fracture toughness and critical energy release rate of ZS5T, ZSTW and ZS5W composites

Composite	Vickers hardness, H (GPa)	Indentation toughness, K_c (MPa $\sqrt{m}$)	Critical energy release rate, G_c (J m^{-2})
ZS5T	19.18 ± 0.71	6.04 ± 0.74	83.30 ± 3.73
ZSTW	19.89 ± 0.65	5.95 ± 1.02	82.09 ± 4.11
ZS5W	17.49 ± 0.74	6.23 ± 0.23	90.49 ± 6.26

Figure 7a–c, respectively, shows the indentation images of ZS5T, ZSTW and ZS5W composites after hardness test under 100 gf load.

Amongst the composites, the minimum indentation fracture toughness of 5.95 ± 1.02 MPa $\sqrt{m}$ was obtained in ZSTW, whereas ZS5T offered slightly higher toughness (6.04 ± 0.74 MPa $\sqrt{m}$). Interestingly, ZS5W recorded the highest indentation toughness of 6.23 ± 0.23 MPa $\sqrt{m}$. In the literature, Chamberlain et al. [11] reported fracture toughness of 4.4 ± 0.2 MPa $\sqrt{m}$ in 99.7% dense ZrB_2–20SiC composite consolidated by hot pressing at 1900 °C for 45 min. In another study, Liu et al. [42] reported a fracture toughness of 4.84 ± 0.28 MPa $\sqrt{m}$ in hot pressed ZrB_2–20SiC–20ZrC (vol.%) composite. Zou et al. [38] found a superior fracture toughness of 5.5 ± 0.5 MPa $\sqrt{m}$ in hot pressed ZrB_2–20SiC–5VC (vol.%) composite. Compared to the published literature, the fracture toughness recorded by the present ZS5T, ZSTW and ZS5W composites is considerably higher. The higher fracture toughness of TiC and WC containing composites can be explained by a possible toughening effect of the matrix due to synergistic reinforcement of SiC, TiC in ZS5T, SiC, TiC and WC in ZSTW, and SiC and WC in ZS5W, respectively. Figure 7d–f, respectively, exhibits the indentation images of ZS5T, ZSTW and ZS5W composites after the indentation toughness test. Evidence of toughening of the matrix can also be observed in Fig. 7g–i, which reveal deflection of diagonal crack emanated from the indentation corner in case of ZS5T, ZSTW and ZS5W, respectively. In addition to crack deflection, crack bridging can also be noticed in Fig. 7. The crack deflection and crack bridging suggest the toughening of the matrix owing to the in situ formation of $(Zr,Ti)B_2$ and $(Zr,W)B_2$ solid solutions. In addition to the formation of core-rim substructure, the maximum fracture toughness in ZS5W may be attributed to the coexistence of hard phases like WB, WC and ZrC with uniform distribution of SiC reinforcement.

The mean critical energy release rate (G_c) of all the composites are found to be in the range 82–90 J m^{-2}, which is higher than that (G_c = 63.0 ± 2.1 J m^{-2}) of ZrB_2–20SiC composite reported in the literature [43]. On the other hand, similar critical energy release rate of 84.9 ± 4.1 J m^{-2} was reported for ZrB_2–20SiC–10CNT (vol.%) [44]. The relatively high G_c also explains for relatively high fracture toughness in TiC and WC containing composites compared to that of ZrB_2–20 vol.% SiC.

Analytical estimation of elastic modulus

In this study, the elastic modulus of sintered ZS5T, ZSTW and ZS5W composites was determined using rule of mixture (ROM), where the theoretical upper

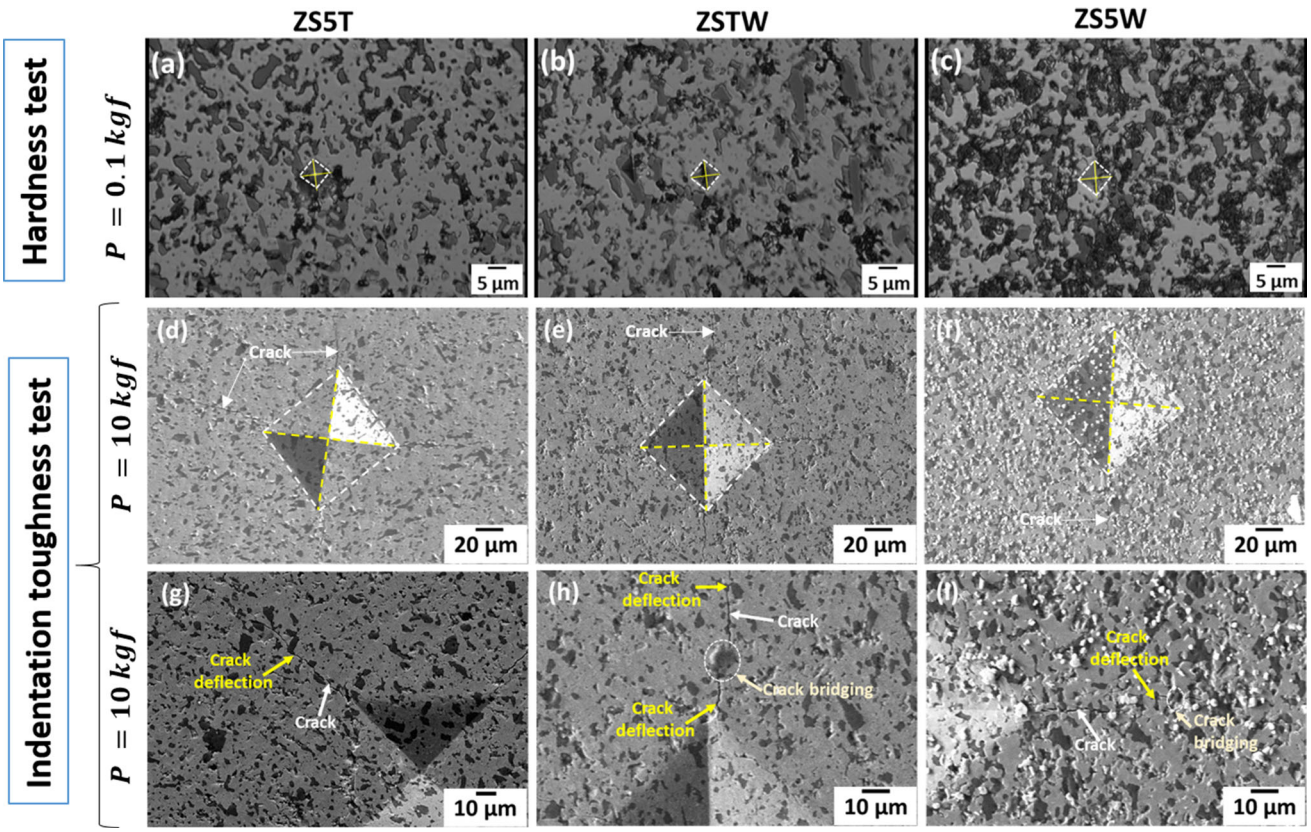

Figure 7 The indentation images of **a** ZS5T, **b** ZSTW and **c** ZS5W composites after hardness testing at 100 gf (= 0.1 kgf) for 10 s. The indentation images of **d** ZS5T, **e** ZSTW and **f** ZS5W composites subjected to indentation toughness test under applied load of 10 kgf. Crack initiation and propagation path from the corners of the indentation diagonal in **g** ZS5T, **h** ZSTW and **i** ZS5W composites may be noted.

(UL) and lower limit (LL) are expressed by Eqs. (11) and (12), as follows:

$$(E_{\mathrm{ROM}})_{\mathrm{UL}} = V_m E_m + V_r E_r \tag{11}$$

$$(E_{\mathrm{ROM}})_{\mathrm{LL}} = \frac{E_m E_r}{V_m E_r + V_r E_m}. \tag{12}$$

In the above equations, E and V represent the elastic modulus and volume fraction and the subscripts 'm' and 'r' indicate the matrix and reinforcement, respectively. However, in a particulate-reinforced composite, the following expression of Voigt–Reuss (VR) model offers more realistic estimation of the elastic modulus since this model considers the random distribution of reinforcement phase in the matrix [23]:

$$E_{\mathrm{VR}} = \frac{3}{8}(E_{\mathrm{ROM}})_{\mathrm{UL}} + \frac{5}{8}(E_{\mathrm{ROM}})_{\mathrm{LL}}. \tag{13}$$

It is noteworthy that ROM and VR models assume the composite to be fully dense. However, in the present study, the composites sintered by SPS did not achieve full densification except in ZS5T. Therefore, it is imperative to consider the effect of residual porosity for realistic estimation of elastic modulus. Equation (14) exhibits the effect of pore volume fraction (V_p) on the elastic modulus (E_p) of a porous composite, as follows:

$$E_p = E_0(1 - aV_p) \tag{14}$$

$$a = \frac{3(9 + 5\upsilon_0)(1 - \upsilon_0)}{2(7 - 5\upsilon_0)}. \tag{15}$$

In Eq. (14), E_0 stands for the upper limit of elastic modulus calculated by rule of mixture ($(E_{\mathrm{ROM}})_{\mathrm{UL}}$), whereas, the relation between constant a and Poisson's ratio of the matrix (υ_0) is expressed in Eq. (15) [13, 45].

Table 6 summarizes the elastic modulus of ZS5T, ZSTW and ZS5W composites by different analytical models. For analytical estimation of elastic modulus of the composites, the elastic modulus of ZrB_2, SiC,

Table 6 Comparison of analytically determined elastic modulus with the modulus obtained by nano-indentation technique in ZS5T, ZSTW and ZS5W composites

Composite	Analytically determined elastic modulus (GPa)				Modulus obtained by nano-indentation technique, E (GPa)
	$(E_{ROM})_{UL}$	$(E_{ROM})_{LL}$	E_{VR}	E_p	
ZS5T	469.58	466.66	467.75	469.58	439.60 ± 39.11
ZSTW	473.30	469.68	471.04	457.59	402.50 ± 48.99
ZS5W	477.03	472.73	474.34	473.71	467.36 ± 40.66

TiC and WC was considered as 489, 401.38, 451 and 600 GPa, [23, 25, 32, 46], respectively. The modulus obtained by nano-indentation, is also presented for comparison. Experimentally, the highest elastic modulus of 467.36 ± 40.66 GPa was obtained in ZS5W. In case of ZSTW, the elastic modulus was found to be relatively low (402.50 ± 48.99 GPa), which may be attributed to the presence of porosity (∼ 1.67%) in sintered ZSTW.

Evaluation of thermal residual stress induced on the composites due to rapid cooling

It is worth noting that the thermal residual stress is induced in ZrB_2-SiC UHTC composites due to the difference in respective coefficients of thermal expansion (CTE) between ZrB_2 ($\alpha = 5.9 \times 10^{-6}$ °C^{-1}) matrix and SiC ($\alpha = 3.5 \times 10^{-6}$ °C^{-1}) reinforcement phases [6, 24, 33]. Literature reports reveal that thermal residual stress is introduced in the composite due to rapid cooling from the sintering temperature in SPS [6, 13, 23, 24, 33]. During fast cooling from SPS temperature, owing to higher α, the matrix phase (ZrB_2) shrinks faster compared to the reinforcement (SiC), which induces compressive residual stress on SiC. As ZS5T, ZSTW and ZS5W contain 5 vol.% of TiC, TiC + WC and WC, respectively, with SiC content remaining the same (20 vol.%), it is logical to evaluate the effect of TiC and/or WC addition on thermal residual stress of these composites. In this study, the effective CTE (α_{eff}) of a composite is determined empirically using the model proposed by Rosen et al. [47]:

$$\alpha_{eff} = f_m\alpha_m + f_r\alpha_r + \frac{(\alpha_m - \alpha_r)}{\left(\frac{1}{K_m} + \frac{1}{K_r}\right)} \cdot \left(\frac{1}{K_{eff}} - \frac{1}{K_m} - \frac{1}{K_r}\right). \tag{16}$$

In a multi-component system, the upper ($(\alpha_{eff})_{UL}$) and lower limit ($(\alpha_{eff})_{LL}$) of CTE depend on multiple factors like shear modulus (G), bulk modulus (K) and volume fraction (f) of matrix (m) and reinforcement (r) phases. In this study, the $(\alpha_{eff})_{UL}$ and $(\alpha_{eff})_{LL}$ are estimated using model developed by Hashin and Shtrikman [48], as shown in Eq. (17) and (18).

$$(\alpha_{eff})_{UL} = \alpha_m - f_r(\alpha_m - \alpha_r)\frac{K_r(3K_m + 4G_m)}{K_m(3K_r + 4G_m) + 4f_rG_m(K_r - K_m)} \tag{17}$$

$$(\alpha_{eff})_{LL} = \alpha_r + f_m(\alpha_r - \alpha_m)\frac{K_m(3K_r + 4G_r)}{K_r(3K_m + 4G_r) + 4f_mG_r(K_m - K_r)}. \tag{18}$$

In order to show the effect of reinforcement phases on the upper and lower limit of CTE in ZS5T, ZSTW and ZS5W composites, the equations are shown in elaborative form in Supplementary material 1.

For analytical estimation of the upper and lower limits of CTE, K of ZrB_2, SiC, TiC and WC was considered as 229, 234, 244 and 630 GPa, respectively [6, 23, 25, 49]. Similarly, the shear modulus (G) of ZrB_2, SiC, TiC and WC was considered as 211, 41, 179 and 274 GPa, respectively [6, 23, 25, 49]. Furthermore, the CTE of ZrB_2, SiC, TiC and WC was taken as 5.9×10^{-6}, 3.5×10^{-6}, 7.4×10^{-6} and 5.5×10^{-6} °C^{-1}, respectively [6, 24, 25, 33]. Table 7 summarizes the theoretically estimated CTE values and thermal residual stresses of the UHTC composites, which shows that the predicted CTE value of the composites decreases with increasing volume fraction of WC. Furthermore, the comparative effect of WC or TiC addition on residual stresses (both compressive and tensile) of sintered composites by SPS appears identical and consistent.

Taya et al. [50] and Hsueh [51] developed different mathematical models to determine the residual stress of matrix and reinforcement phases in a composite

Table 7 The coefficient of thermal expansion of the composite, the thermal residual stress of the composites by Hsueh's model, Biaxial residual stress and Taya's model

Composite	Coefficient of thermal expansion, α ($\times 10^{-6}$ °C^{-1})			Thermal residual stress (GPa)				
	$(\alpha_{eff})_{UL}$	$(\alpha_{eff})_{LL}$	α_{ROM}	Hsueh's model	Biaxial residual stress	Taya's model		Average compressive stress on SiC grains (by Raman analysis)
						σ_m	σ_r	
ZS5T	5.49	3.07	5.50	0.65	1.39	0.22	− 0.65	− 0.68
ZSTW	5.41	2.75	5.45	0.74	1.55	0.26	− 0.73	− 0.78
ZS5W	5.34	2.44	5.40	0.84	1.71	0.28	− 0.84	− 0.82

The average compressive stress on SiC grains, as estimated using Raman spectroscopy, is also presented for comparison

aggregate and several studies [23, 43] have utilized both Taya's model and Hsueh's model to estimate the residual stress of ceramic matrix composites. Accordingly, the residual stress of reinforcement and matrix phases in the present composites has been estimated empirically using both these models. It may be noted that Taya's model considers the effect of porosity (f_v), Poisson's ratio (v), volume fraction of reinforcement (f_r) and elastic modulus (E) on residual stress (σ) of matrix (m) and reinforcement (r) phases through Eqs. (19)–(22), as follows:

$$\beta = \left(\frac{1+v_m}{1-2v_r}\right)\left(\frac{E_r}{E_m}\right) \tag{19}$$

$$\sigma_m = \frac{2f_r\beta\varepsilon'}{(1-f_v)\left[\left(1-\frac{f_r}{1-f_v}\right)(\beta+2)(1+v_m)+\frac{3\beta f_r(1-v_m)}{1-f_v}\right]}.E_m \tag{20}$$

$$\sigma_r = -\frac{2(1-f_r-f_v)\beta\varepsilon'}{(1-f_v)\left[\left(1-\frac{f_r}{1-f_v}\right)(\beta+2)(1+v_m)+\frac{3\beta f_r(1-v_m)}{1-f_v}\right]}.E_m \tag{21}$$

$$\varepsilon' = \Delta\alpha\cdot\Delta T = (\alpha_m-\alpha_r)\Delta T. \tag{22}$$

The detailed equations for determination of thermal residual stress of ZS5T, ZSTW and ZS5W composites are provided in Supplementary Material 1. Equation (22) expresses the relation between thermally induced strain (ε') with difference in CTE ($\Delta\alpha$) and temperature (ΔT). According to Taya's model, the tensile residual stress of the matrix and the compressive residual stress of the reinforcement is found to increase with WC content. The maximum tensile residual stress of 0.28 GPa and minimum compressive stress of –0.84 GPa were observed in the matrix and reinforcement of ZS5W, respectively.

As earlier stated, the thermal residual stress of ZS5T, ZSTW and ZS5W composites has also been estimated using Hsueh's model [52]:

$$\sigma = \frac{(\alpha_m-\alpha_r)\Delta T}{\frac{1+v_m}{(1+v_r)E_m}+\frac{1-2v_r}{E_r}} \tag{23}$$

The biaxial residual stress is estimated in accordance with Eq. (24) [53]:

$$\sigma = \left(\frac{E_m}{1-v_m}\right)\varepsilon' \tag{24}$$

According to Eqs. (23) and (24), the residual stress of the composite is found to increase with the volume fraction of WC. This observation corroborates with the residual stress values estimated by Taya's model.

In this study, the residual stress of SiC reinforcement phase is determined experimentally with the help of Raman spectroscopy and compared with the predicted residual stress by Taya's model. However, it is extremely important to mention that the actual residual stress of the composite may differ from the thermal residual stress determined by Raman analysis as the latter is primarily a surface-sensitive analytical tool. Since ZrB_2 is not Raman active, the residual stress of the matrix phase could not be determined using Raman spectroscopy. In the past, Watt et al. [54] estimated thermal residual stress of SiC in sintered ZrB_2-SiC using Raman Spectroscopy. In a recent study [13], the present authors also utilized Raman spectroscopy to determine residual stress of SiC in ZrB_2–SiC–AlSiMg and ZrB_2–SiC composites. In case of 6H–SiC, the characteristic peak

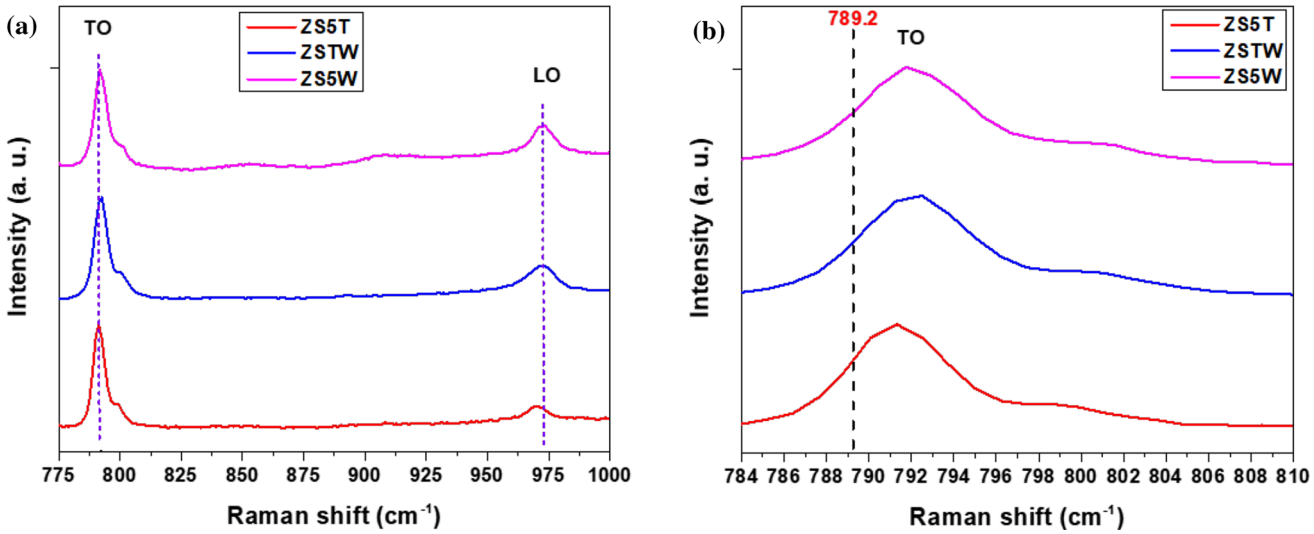

Figure 8 Raman analysis elicits the characteristic TO and LO peaks of SiC in **a** ZS5T, ZSTW and ZS5W. **b** Exhibits the shift of TO peak. The ideal TO peak position at 789.2 cm^{-1} is shown for reference.

positions of transverse optical (TO) longitudinal optical (LO) shifts are obtained at the respective wave numbers of 789.2 and 970.1 cm^{-1} [55]. Ghosh et al. [56] reported that the shift of the characteristic TO and LO peaks towards respective higher or lower wave numbers implies the evolution of compressive or tensile stress in the SiC grains.

Figure 8 shows the representative TO and LO peak positions of SiC in ZS5T, ZSTW and ZS5W composites. The peak positions are found to be sensitive to TiC and WC content. In this study, the characteristic peak position of TO was obtained by taking Raman spectra on different SiC grains on each composite. The mean value of TO peak position of SiC was found to be 791.30, 791.62 and 791.74 cm^{-1} in case of ZS5T, ZSTW and ZS5W, respectively. Therefore, in all cases, the TO peak positions are shifted towards higher wave numbers, revealing that compressive stress is induced on SiC grains. Watt et al. [57] reported that the magnitude of the compressive stress (P) can be determined from the peak shift of TO (i.e. ΔTO) using the following equation:

$$P = \frac{3.11 - \sqrt{9.6721 - 0.036(\Delta TO)}}{0.018}. \quad (25)$$

Based on the above analysis, the average value of compressive residual stress of SiC was found to be –0.68, –0.78 and –0.82 GPa, respectively, which is in good agreement with the residual stress of reinforcement estimated by Taya's model. The entire spectrum of important physical and mechanical properties, as discussed above, are summarized in Table 7.

Nano-mechanical properties

Of late, different research groups have utilized nano-indentation technique to evaluate the mechanical behaviour of ZrB_2-based composites, especially of the surface or thin films, under low load and elastic strain regime [13, 58]. In the present work, nano-hardness and indentation modulus of ZS5T, ZSTW and ZS5W composites have been determined by nano-indentation technique utilizing the well-established Oliver–Pharr method [34]. Table 8 summarizes the critical aspects of nano-mechanical behaviour of sintered (by SPS) ZS5T, ZSTW and ZS5W composites under identical loading and unloading conditions. The representative load–displacement ($P - h$) curves of the sintered composites are recorded in Fig. 9a. For clarity, the selected region of Fig. 9a is magnified and shown in Fig. 9b. From the nano-indentation data, the resistance to deformation (r_d) and plasticity index (r_e) have been calculated in accordance with Eqs. (26) and (27), respectively:

$$r_d = \frac{h_f}{h_{\max}} \quad (26)$$

$$r_e = \frac{h_{\max} - h_f}{h_{\max}}. \quad (27)$$

Here, h_f and $h_{\max}$ represent the final and maximum indentation depth values, respectively. From Table 8

Table 8 The important nano-mechanical behaviour of spark plasma-sintered ZS5T, ZSTW and ZS5W composites

Composite	Nano-hardness (GPa)	Indentation modulus, E (GPa)	The maximum penetration depth, h_{max} (nm)	The final depth, h_f (nm)	$\frac{h_f}{h_{max}}$	$1-\frac{h_f}{h_{max}}$	Stiffness,S (mN nm^{-1})
ZS5T	19.65 ± 2.57	439.60 ± 39.11	1098.98 ± 61.22	763.03 ± 64.59	0.69 ± 0.03	0.31 ± 0.03	1.90 ± 0.10
ZSTW	19.68 ± 3.49	402.50 ± 48.99	1128.10 ± 67.55	750.58 ± 74.30	0.66 ± 0.04	0.34 ± 0.04	1.61 ± 0.17
ZS5W	17.27 ± 2.72	467.36 ± 40.66	1105.39 ± 43.42	770.50 ± 53.23	0.71 ± 0.04	0.29 ± 0.04	2.12 ± 0.12

and Fig. 9, it is evident that the penetration depth, final depth, nano-hardness and indentation modulus are sensitive to TiC and WC content in the poly-crystalline composite aggregates. The nano-hardness of ZSTW (H = 19.68 ± 3.49 GPa) and ZS5T (H = 19.65 ± 2.57 GPa) are found to be similar and close to the highest mark, while the H value (= 17.27 ± 2.72 GPa) is the minimum for ZS5W composite containing 5 vol.% WC. As the hardness of WC (18–22 GPa [25]) is lower than that of TiC (28–35 GPa [24]), ZS5W is expected to offer relatively lower hardness. This observation is in line with the results obtained by Vickers hardness testing (Table 5). Furthermore, the minimum value of the highest penetration depth (h_{max} = 1098.98 ± 61.22 nm) is recorded in ZS5T, whereas, the maximum h_{max} of 1128.10 ± 67.55 nm was offered by ZSTW. Interestingly, ZSTW offers the minimum value of the final depth (h_f = 750.58 ± 74.30 nm) as well. Accordingly, the minimum resistance to deformation and maximum plasticity index was also observed in ZSTW.

The change in modulus of UHTC composites is also reflected by the alteration in stiffness (S), computed from the unloading section of $P-h$ curve (Table 8). The highest S of 2.12 ± 0.12 mN nm^{-1} was obtained in ZS5W, which was followed by that of ZS5T (S = 1.90 ± 0.10 mN nm^{-1}) and ZSTW (S = 1.61 ± 0.17 mN nm^{-1}). It may be noted that, the average indentation modulus of ZS5W, ZS5T and ZSTW was found to be 467.36, 439.60 and 402.50 GPa was, respectively. As indicated by the theoretical estimation of elastic moduli in "Effect of TiC and WC addition on hardness and fracture toughness" section, slight reduction in the indentation modulus of ZSTW may be ascribed to the presence of porosity (~ 1.67%) in sintered ZSTW composite. In this connection, it is important to mention that, the elastic modulus of WC (E = 600 GPa [25]) is comparatively higher than that of TiC (E = 410–510 GPa [24]). Therefore, ZrB_2–20SiC–5WC (ZS5W) composite offers relatively higher modulus as compared to that of ZrB_2–20SiC–5TiC (ZS5T).

Reciprocating wear behaviour of ZS5T, ZSTW and ZS5W composites

Several research groups have examined the wear behaviour of sintered UHTC composites using scratch test [59], fretting test [26], ball-on-disc rotating wheel wear test [60] or linear reciprocating wear test [61]. In this study, the wear behaviour of spark plasma-sintered UHTC composites was examined by reciprocating wear test in ambient condition. Figure 10a–c, respectively, shows the optical profilometry images of single wear tracks of ZS5T, ZSTW and ZS5W composites. The mean coefficient of fraction (COF) of ZS5T, ZSTW and ZS5W were found to be 0.49, 0.47 and 0.50, respectively. These values suggest that there is no significant effect of WC and/or TiC on COF of the sintered composites. During linear reciprocating wear test, the wear debris are formed on top of the worn surfaces owing to sliding of the counter body (WC-Co, in this study). The wear debris formed during the reciprocating wear tests are compacted and welded into formation of a tribo-layer during extended wear tests. As a result, SEM images reveal that the wear tracks of ZS5T (Fig. 10d, g), ZSTW (Fig. 10e, h) and ZS5W (Fig. 10f, i) composites are covered with this tribo-layer. The evidence of grain pull-out and wear debris is also indicated in Fig. 10g–i. Similar microstructural investigation at higher magnification shows evidences of delamination in the wear tracks, which indicates that abrasive wear is the primary mechanism of material loss during reciprocating wear test of these composites.

Figure 11a–c reveals the representative EDS elemental compositional maps of the selected regions of wear tracks. These elemental maps provide definite evidences of material transfer or inter-diffusion between the sliding bodies (i.e. UHTC composites

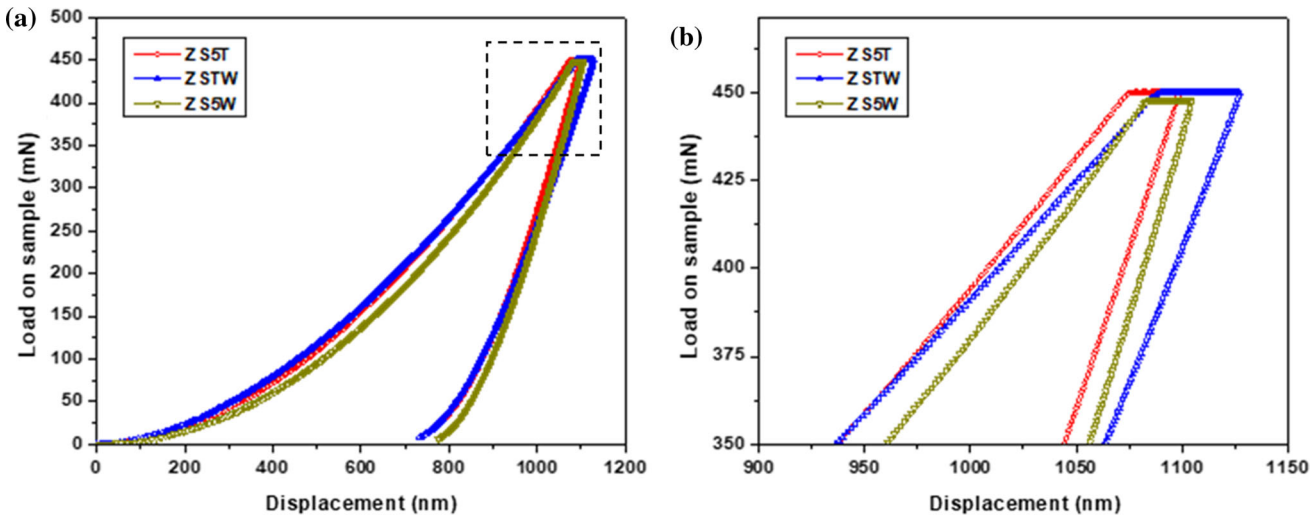

Figure 9 Representative nano-indentation curve of the sintered ZS5T, ZSTW and ZS5W composites. **b** Is the magnified view of the dotted region of **a**.

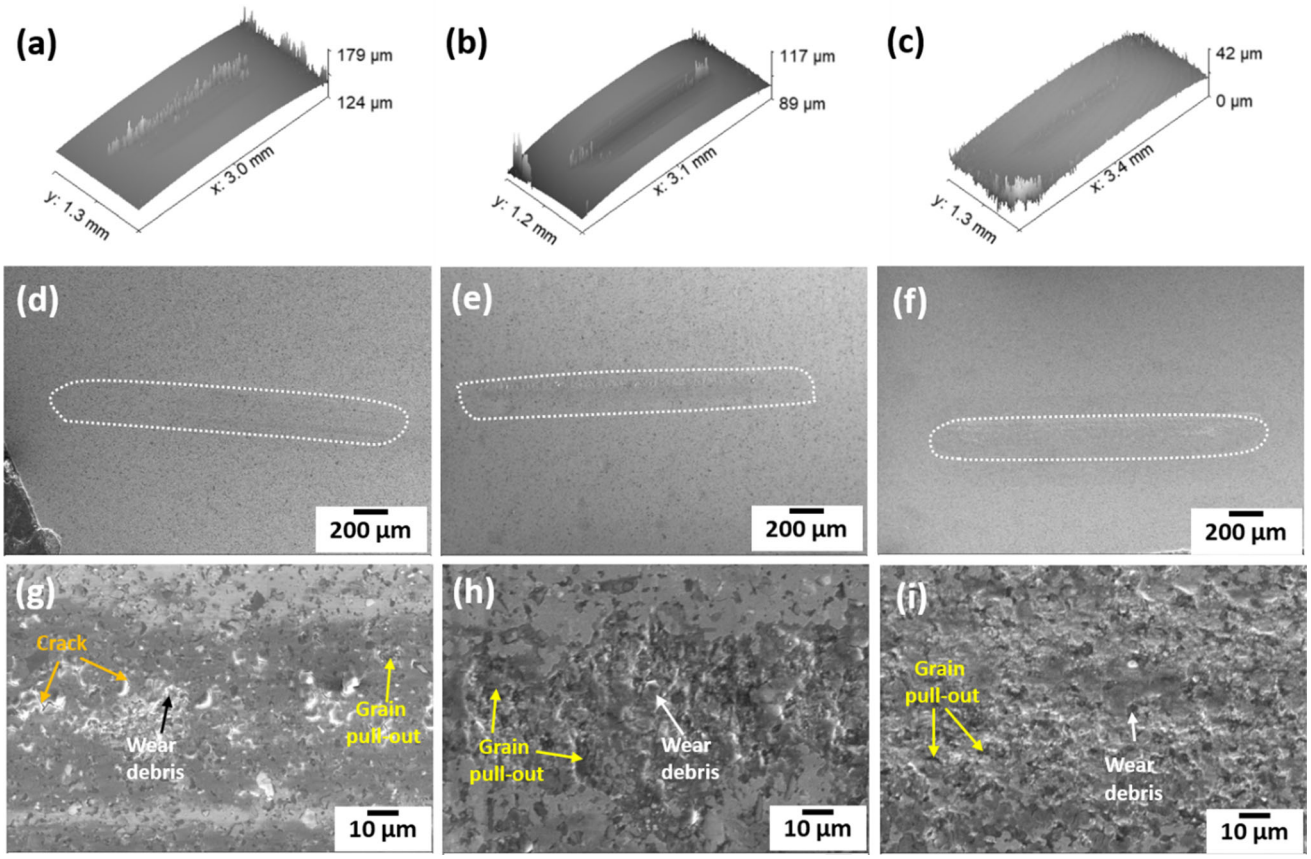

Figure 10 Optical profilometry of the single wear tracks in **a** ZS5T, **b** ZSTW and **c** ZS5W composites after reciprocating wear test. SEM images of wear tracks of **d**, **g** ZS5T, **e**, **h** ZSTW and **f**, **i** ZS5W composites.

and WC counter body) and formation of tribo-layers on the wear tracks. In case of ZS5T (Fig. 11a), the presence of Zr, B, Si, C and Ti (from composite) and W and C (from ball) was detected. In addition, the presence of oxygen was noticed which hints at localized oxidation of the sample during the wear

test. Similar incidence of tribooxidation has also been reported by Savchenko et al. [62] on the worn surfaces of ZrB_2–20SiC (vol.%) composites after high speed sliding wear experiments. Figure 11b shows the distribution of Zr, B, Si, C, Ti and W (from ZSTW composite), W and C (from WC counter body) and O in the wear track, respectively. Similarly, Fig. 11c records the presence of Zr, B, Si, C and W (from ZS5W composite), W and C (from WC ball) and O in the wear track of ZS5W composite, respectively.

The wear volume (W_V) was calculated from the geometrical data of the wear track obtained by optical profilometry and is presented in Table 9. The minimum wear volume of $(6.18 \pm 0.40) \times 10^{-3}$ cm^3 was recorded in case of ZS5W, while the maximum wear volume of $(8.66 \pm 1.94) \times 10^{-3}$ cm^3 was observed in 2.5 vol.% WC and TiC containing ZSTW composite. The experimental wear rate ($W_{r\,exp}$) was determined from the calculated wear volume according to the following equation:

$$W_{r\,exp} = \frac{W_V}{F_N L n}. \tag{28}$$

In Eq. (27), F_N, L and n represent the normal load, sliding distance and total number of cycles, respectively. The maximum wear rate of $(3.23 \pm 0.15) \times 10^{-6}$ $cm^3N^{-1}\,m^{-1}$ was obtained in ZSTW, while the minimum wear rate of $(2.58 \pm 0.17) \times 10^{-6}$ $cm^3N^{-1}\,m^{-1}$ was recorded in ZS5W. On the other hand, ZS5T composite, which contains 5 vol.% TiC, offers intermediate wear volume (= $(7.61 \pm 0.91) \times 10^{-3}$ cm^3) and wear rate (= $(3.17 \pm 0.38) \times 10^{-6}$ $cm^3N^{-1}\,m^{-1}$). Owing to the synergistic reinforcement of TiC and/or WC with SiC and the corresponding increase in hardness and fracture toughness, ZS5T, ZSTW and ZS5W composites record much low wear rate compared to the base ZrB_2–20 vol.% coarse SiC (= 3×10^{-3} $cm^3N^{-1}\,m^{-1}$) and ZrB_2–20 vol.% fine SiC (= 6×10^{-4} $cm^3N^{-1}\,m^{-1}$) [63] composites, which were subjected to ball-on-disc wear test under normal load of 10 N for 10 min maintaining an RPM of 20. In order to assess the relative effect of TiC and WC addition, the Archard equation constant (k) [64] was determined from Eq. (29) and is shown in Table 9.

$$\Delta W_V = k\frac{F_s}{H_V}\Delta x. \tag{29}$$

In Eq. (29), Δx stands for the sliding distance.

The minimum value of k $(=(4.93 \pm 0.32) \times 10^{-4})$ was obtained for ZS5W, which was followed by ZS5T $(k=(5.60 \pm 0.18) \times 10^{-4})$ and ZSTW $(k=(6.26 \pm 0.75) \times 10^{-4})$, indicating that ZS5W offers the maximum resistance to wear loss despite the identical wear conditions.

The fracture toughness exponent (a) [65] is correlated with the wear volume (W_V), hardness (H_V) and fracture toughness (K_c) of the material according to the following equation:

$$a = -\frac{\ln\left(W_V H_V^b\right)}{\ln K_c}. \tag{30}$$

The exponent b is considered to be 1.5 for ceramic materials [65]. The highest fracture toughness exponent ($a = 0.37 \pm 0.04$) was recorded by ZS5W, whereas ZSTW offers the minimum value of a $(= 0.22 \pm 0.07)$. Lower value of fracture toughness exponent implies the higher wear volume loss. This explains the reason behind relatively high wear volume loss in ZSTW. The following equation provides the mathematical expression of brittleness index, which is important to perform qualitative assessment of wear behaviour of material:

$$\text{Brittleness index(BI)} = \frac{H}{K_c}. \tag{31}$$

The mean brittleness index of ZS5W was ~ 17.4% and ~ 15.4% less than that of ZSTW and ZS5T, respectively. Both the fracture toughness exponent and brittleness index indicate that ZS5W offers the minimum wear loss or best wear resistance under the present experimental conditions when compared with its counterparts. In addition to wear volume, Table 9 summarizes the coefficient of friction, experimental wear rate, brittleness index, Archard equation constant and fracture toughness exponent of the composites.

From the SEM images, the average track width in ZS5T, ZSTW and ZS5W was found to be ~ 422, ~ 456 and ~ 367 μm, respectively. The optical profilometry images indicate that the wear depth of ZSTW is the highest followed by that of ZS5T and ZS5W. When stroke length (= 2 mm) is fixed, the higher track width and wear track depth in ZSTW invariably indicates that the wear rate of ZSTW is higher than that of its counterpart. This observation is in line with the calculated value of experimental wear rate, which shows that the wear rate of the present composites follows the order: $(W_{r\,exp})_{ZS5W} < (W_{r\,exp})_{ZS5T} < (W_{r\,exp})_{ZSTW}$.

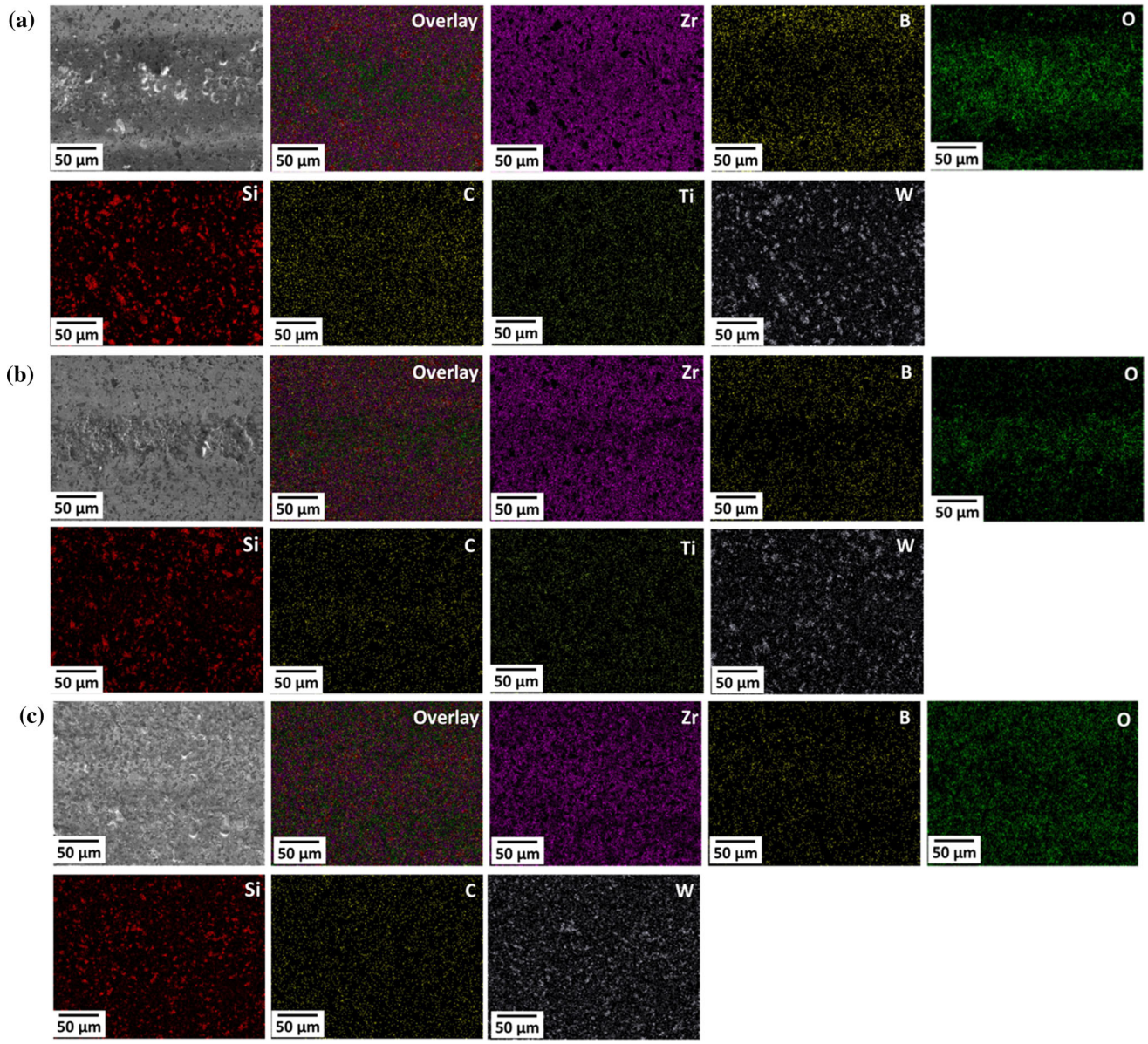

Figure 11 EDS elemental map showing the formation of tribo-layer in the wear tracks of **a** ZS5T, **b** ZSTW and **c** ZS5W.

Table 9 The coefficient of friction, wear volume, experimental wear rate, Archard equation constant and fracture toughness exponent of UHTC composites under consideration

Composite	Coefficient of friction	Wear volume ($\times 10^{-3}$ cm^3)	Experimental wear rate ($\times 10^{-6}$ cm^3 N^{-1} m^{-1})	Brittleness index ($\times 10^3$ $m^{-1/2}$) H/K_c	Archard equation constant ($\times 10^{-4}$), k	Fracture toughness exponent, a
ZS5T	0.49 ± 0.06	7.61 ± 0.91	3.17 ± 0.38	3.32 ± 0.37	5.60 ± 0.18	0.26 ± 0.03
ZSTW	0.47 ± 0.08	8.66 ± 1.94	3.23 ± 0.15	3.40 ± 0.53	6.26 ± 0.75	0.22 ± 0.07
ZS5W	0.50 ± 0.05	6.18 ± 0.40	2.58 ± 0.17	2.84 ± 0.26	4.93 ± 0.32	0.37 ± 0.04

Conclusions

In this study, the relative influence of TiC and WC addition on densification, phase, microstructure, mechanical properties, residual stress and wear behaviour has been investigated in spark plasma-sintered ZrB_2–SiC composite. Based on the results presented in this study, the following conclusions are drawn:

(a) Spark plasma-sintered ZrB_2–20SiC–5TiC (vol.%) composites consolidated at 1700 °C for 5 min achieve 99.6% sintered density. However, addition of WC leads to relatively poor densification under the same sintering cycle. When sintered at 1800 °C for 10 min under 70 MPa pressure, WC containing ZrB_2–20SiC–2.5TiC–2.5WC (vol.%) and ZrB_2–20SiC–5WC (vol.%) achieve mean relative density of 98.33% and 99.65% (theoretical), respectively.

(b) XRD and SEM–EDS analyses substantiate that no unreacted TiC is present in sintered ZrB_2-20SiC-5TiC (vol.%) composite. Instead, in situ formation of (Zr,Ti)B_2 solid solution could be confirmed. The evolution of core–shell substructure is noticed in ZrB_2–20SiC–5WC (vol.%) composite. WC containing composites (ZrB_2–20SiC–2.5TiC–2.5WC, ZrB_2–20SiC–5WC) exhibit the presence of free or unreacted WC in addition to the in-situ evolution of ZrC, WB and (Zr,W)B_2 phases.

(c) The rule of mixture applied to the Hashin and Shtrikman model indicated that coefficient of thermal expansion of the sintered composite decrease with increasing WC content. The theoretically estimated and experimentally determined thermal residual stress are found to be in good agreement. The incorporation of WC increases the residual stress of the matrix and reinforcement phases.

(d) Owing to the combined effect of solid solution strengthening, dispersion strengthening and in situ formation of ZrC and WB phases, ZrB_2–20SiC–2.5TiC–2.5WC composite records the maximum hardness (19.89 ± 0.65 GPa), whereas, 5 vol.% WC containing composite offers an excellent combination of indentation toughness (6.23 ± 0.23 MPa $\sqrt{m}$), indentation modulus (467.36 ± 40.66 GPa) and critical energy release rate (90.49 ± 6.26 J m^{-2}).

(e) Abrasive wear is the most significant mechanism during the reciprocating wear test of the sintered composites. Due to desirable combination of low brittleness index ((2.84 ± 0.26) × 10^3 $m^{-1/2}$) and high fracture toughness exponent (0.37 ± 0.04), 5 vol.% WC containing ZrB_2-20SiC-5WC composite records the minimum wear loss ((6.18 ± 0.40) × 10^{-3} cm^3) and minimum wear rate ((2.58 ± 0.17) × 10^{-6} cm^{3-} N^{-1} m^{-1}) under the same experimental conditions. SEM–EDS analysis confirmed that the linear reciprocating wear test caused material transfer between the specimen and the counter body and gave rise to the formation of tribolayer on wear tracks.

Overall, the incorporation of both TiC and WC is found to be beneficial in ZrB_2–SiC system. For densification, WC containing composites necessitate higher temperature (1800 °C or more) in spark plasma sintering route. The composites containing TiC offered excellent hardness, whereas 5 vol.% WC containing ZrB_2–20SiC–5WC composite records the highest toughness and modulus and provides the best resistance to wear.

Acknowledgements

I.M. would like to acknowledge partial financial support from DST sponsored projects 'JCP' and 'DGL', and ISRO sponsored project 'ONC'. PS wants to acknowledge financial support from CSIR-IMMT sponsored project 'OLP-76'. IIT Kharagpur and ARCI Hyderabad are acknowledged for spark plasma sintering facility. Central Characterization Department, CSIR-IMMT is gratefully acknowledged for various characterization facilities. Help from Mr. Nigamananda Ray, CSIR-IMMT is acknowledged for carrying out the thermodynamic analysis using the HSC Chemistry software. Special thanks are due to Mr. D. Krishna Reddy for high-energy ball milling and Mr. G. Padma Rao for reciprocating wear test and SEM analysis.

Author contributions

PS contributed to conceptualization, data curation, formal analysis, investigation, methodology and roles/writing—original draft. SB contributed to funding acquisition, resources and supervision. IM

contributed to conceptualization, funding acquisition, resources, supervision, validation, visualization and writing—review and editing.

Declarations

Conflict of interest The authors declare that they have no conflict of interest.

Supplementary Information: The online version contains supplementary material available at https://doi.org/10.1007/s10853-022-08021-x.

References

[1] Johnson SM (2016) Thermal protection materials and systems: an overview. In: Ohji T, Singh M (eds) Engineered ceramics: current status and future prospects, 1st edn. Wiley, pp 224–243

[2] Johnson SM (2018) Thermal protection materials and systems: past, present, and future

[3] Sengupta P, Manna I (2019) Advanced high-temperature structural materials for aerospace and power sectors: a critical review. Trans Indian Inst Met 72:2043–2059. https://doi.org/10.1007/s12666-019-01598-z

[4] Nayebi B, Delbari SA, Shahedi Asl M et al (2021) A nanostructural approach to the interfacial phenomena in spark plasma sintered TiB2 ceramics with vanadium and graphite additives. Compos Part B Eng 222:109069. https://doi.org/10.1016/j.compositesb.2021.109069

[5] Sengupta P, Manna I (2022) Advanced high-temperature structural materials in petrochemical, metallurgical, power, and aerospace sectors—an overview. In: Bhattacharjee D, Chakrabarti S (eds) Future landscape of structural materials in India. Springer, Singapore, pp 79–131

[6] Fahrenholtz WG, Hilmas GE, Talmy IG, Zaykoski JA (2007) Refractory diborides of zirconium and hafnium. J Am Ceram Soc 90:1347–1364. https://doi.org/10.1111/j.1551-2916.2007.01583.x

[7] Monteverde F, Bellosi A, Scatteia L (2008) Processing and properties of ultra-high temperature ceramics for space applications. Mater Sci Eng A 485:415–421. https://doi.org/10.1016/j.msea.2007.08.054

[8] Inoue R, Arai Y, Kubota Y et al (2018) Oxidation of ZrB2 and its composites: a review. J Mater Sci 53:14885–14906. https://doi.org/10.1007/s10853-018-2601-0

[9] Chamberlain AL, Fahrenholtz WG, Hilmas GE (2006) Pressureless sintering of zirconium diboride. J Am Ceram Soc 89:450–456. https://doi.org/10.1111/j.1551-2916.2005.00739.x

[10] Zapata-solvas E, Jayaseelan DD, Lin HT et al (2013) Mechanical properties of ZrB2- and HfB2-based ultra-high temperature ceramics fabricated by spark plasma sintering. J Eur Ceram Soc 33:1373–1386. https://doi.org/10.1016/j.jeurceramsoc.2012.12.009

[11] Chamberlain AL, Fahrenholtz WG, Hilmas GE, Ellerby DT (2004) High strength ZrB2-based ceramics. J Am Ceram Soc 87:1170–1172

[12] Cao M, Wang S, Han W (2010) Influence of nanosized SiC particle on the fracture toughness of ZrB2-based nanocomposite ceramic. Mater Sci Eng A 527:2925–2928. https://doi.org/10.1016/j.msea.2010.01.059

[13] Sengupta P, Basu S, Manna I (2021) Structure–property correlation in a novel ZrB2–SiC ultrahigh-temperature ceramic composite with Al-alloy sinter additive. J Mater Sci 56:19029–19046. https://doi.org/10.1007/s10853-021-06427-7

[14] Sharma A, Karunkar DB (2022) Effect of SiC and MgO addition on mechanical and ablation characteristics of spark plasma sintered ZrB2 -based composites. J Mater Sci 57:15354–15373. https://doi.org/10.1007/s10853-022-07587-w

[15] Guo S (2018) Effects of VC additives on densification and elastic and mechanical properties of hot-pressed ZrB2–SiC composites. J Mater Sci 53:4010–4021. https://doi.org/10.1007/s10853-017-1850-7

[16] Mallik M, Ray KK, Mitra R (2017) Effect of Si3N4 addition on oxidation resistance of ZrB2-SiC composites. Coatings 7:1–9. https://doi.org/10.3390/coatings7070092

[17] Guo SQ, Kagawa Y, Nishimura T, Tanaka H (2008) Pressureless sintering and physical properties of ZrB2-based composites with ZrSi2 additive. Scr Mater 58:579–582. https://doi.org/10.1016/j.scriptamat.2007.11.019

[18] Shahedi M, Nayebi B, Motallebzadeh A (2019) Nanoindentation and nanostructural characterization of ZrB2–SiC composite doped with graphite nano-flakes. Compos Part B 175:107153. https://doi.org/10.1016/j.compositesb.2019.107153

[19] Monteverde F, Silvestroni L (2016) Combined effects of WC and SiC on densification and thermo-mechanical stability of ZrB2 ceramics. Mater Des 109:396–407. https://doi.org/10.1016/j.matdes.2016.06.114

[20] Zou J, Zhang GJ, Hu CF et al (2012) Strong ZrB2-SiC-WC ceramics at 1600°C. J Am Ceram Soc 95:874–878. https://doi.org/10.1111/j.1551-2916.2011.05062.x

[21] Zhang SC, Hilmas GE, Fahrenholtz WG (2008) Improved oxidation resistance of zirconium diboride by tungsten carbide additions. J Am Ceram Soc 91:3530–3535. https://doi.org/10.1111/j.1551-2916.2008.02713.x

[22] Silvestroni L, Kleebe HJ, Fahrenholtz WG, Watts J (2017) Super-strong materials for temperatures exceeding 2000 °C. Sci Rep 7:1–8. https://doi.org/10.1038/srep40730

[23] Sengupta P, Sahoo SS, Bhattacherjee A et al (2020) Effect of TiC addition on structure and properties of spark plasma sintered ZrB2–SiC–TiC ultrahigh temperature ceramic composite. J Alloys Compd 850:156668. https://doi.org/10.1016/j.jallcom.2020.156668

[24] Pierson HO (1996) Handbook of refractory carbides and nitrides: properties, characteristics, processing, and application. Noyes Publications, New York

[25] Kurlov AS, Gusev AI (2013) Tungsten carbides: structure properties and application in hardmetals. Springer, Berlin

[26] Nisar A, Balani K (2017) Role of interfaces on multi-length scale wear mechanics of TaC-based composites. Adv Eng Mater 19:1–10. https://doi.org/10.1002/adem.201600713

[27] Zou J, Rubio V, Binner J (2017) Thermoablative resistance of ZrB2-SiC–WC ceramics at 2400 °C. Acta Mater 133:293–302. https://doi.org/10.1016/j.actamat.2017.05.033

[28] Golla BR, Mukhopadhyay A, Basu B, Thimmappa SK (2020) Review on ultra-high temperature boride ceramics. Prog Mater Sci 111:100651. https://doi.org/10.1016/j.pmatsci.2020.100651

[29] Anstis GR, Chantikul P, Lawn BR, Marshall DB (1981) A Critical evaluation of indentation techniques for measuring fracture toughness: I, direct crack measurements. J Am Ceram Soc 64:533–538. https://doi.org/10.1111/j.1151-2916.1981.tb10320.x

[30] Sciti D, Guicciardi S, Nygren M (2008) Densification and mechanical behavior of HfC and HfB2 fabricated by spark plasma sintering. J Am Ceram Soc 91:1433–1440. https://doi.org/10.1111/j.1551-2916.2007.02248.x

[31] Yan X, Jin X, Li P et al (2019) Microstructures and mechanical properties of ZrB2–SiC–Ni ceramic composites prepared by spark plasma sintering. Ceram Int 45:16707–16712. https://doi.org/10.1016/j.ceramint.2019.05.151

[32] Shackelford JF, Han Y-H, Kim S, Kwon S-H (2016) CRC materials science and engineering handbook, 4th edn. CRC Press, Boca Raton

[33] Ariharan S, Sengupta P, Nisar A et al (2017) Dual-layer oxidation-protective plasma-sprayed SiC–ZrB2/Al2O3–carbon nanotube coating on graphite. J Therm Spray Technol 26:417–431. https://doi.org/10.1007/s11666-016-0508-3

[34] Oliver WC, Pharr GM (1992) An improved technique for determining hardness and elastic modulus using load and displacement sensing indentation experiments. J Mater Res 7:1564–1583. https://doi.org/10.1557/jmr.1992.1564

[35] Cullity BD (1956) Elements of X-ray diffraction. Addison-Wesley Publishing Company, INC., Notre Dame

[36] Turchanin MA, Agraval PG, Abdulov AR (2008) Thermodynamic assessment of the Cu–Ti–Zr system. II. Cu–Zr and Ti–Zr systems. Powder Metall Met Ceram 47:428–446. https://doi.org/10.1007/s11106-008-9039-x

[37] Ghasali E, Shahedi Asl M (2018) Microstructural development during spark plasma sintering of ZrB2–SiC–Ti composite. Ceram Int 44:18078–18083. https://doi.org/10.1016/j.ceramint.2018.07.011

[38] Zou J, Zhang GJ, Kan YM, Wang PL (2009) Hot-pressed ZrB2-SiC ceramics with VC addition: chemical reactions, microstructures, and mechanical properties. J Am Ceram Soc 92:2838–2846. https://doi.org/10.1111/j.1551-2916.2009.03293.x

[39] Ahmadi Z, Nayebi B, Shahedi Asl M et al (2017) Sintering behavior of ZrB2–SiC composites doped with Si3N4: a fractographical approach. Ceram Int 43:9699–9708. https://doi.org/10.1016/j.ceramint.2017.04.144

[40] Silvestroni L, Sciti D (2007) Effects of MoSi2 additions on the properties of Hf- and Zr-B2 composites produced by pressureless sintering. Scr Mater 57:165–168. https://doi.org/10.1016/j.scriptamat.2007.02.040

[41] Callister WD, Rethwisch DG (2013) Callister's materials science and engineering (Adapted by R. Balasubramaniam), 2nd edn. Wiley, New York

[42] Liu HL, Zhang GJ, Liu JX, Wu H (2015) Synergetic roles of ZrC and SiC in ternary ZrB2-SiC-ZrC ceramics. J Eur Ceram Soc 35:4389–4397. https://doi.org/10.1016/j.jeurceramsoc.2015.08.024

[43] Nisar A, Balani K (2017) Phase and microstructural correlation of spark plasma sintered HfB2-ZrB2 based ultra-high temperature ceramic composites. Coatings 7:110. https://doi.org/10.3390/coatings7080110

[44] Nisar A, Ariharan S, Balani K (2017) Establishing microstructure-mechanical property correlation in ZrB2-based ultra-high temperature ceramic composites. Ceram Int 43:13483–13492. https://doi.org/10.1016/j.ceramint.2017.07.053

[45] Choren JA, Heinrich SM, Silver-Thorn MB (2013) Young's modulus and volume porosity relationships for additive manufacturing applications. J Mater Sci 48:5103–5112. https://doi.org/10.1007/s10853-013-7237-5

[46] Cutler RA (1991) Engineering properties of borides in ceramics and glasses: engineered materials handbook, vol 4. ASM International, Materials Park

[47] Rosen BW, Hashin Z (1970) Effective thermal expansion coefficients and specific heats of composite materials. Int J Eng Sci 8:157–173. https://doi.org/10.1016/0020-7225(70)90066-2

[48] Hashin Z, Shtrikman S (1963) A variational approach to the theory of the elastic behaviour of multiphase materials. J Mech Phys Solids 11:127–140. https://doi.org/10.1016/0022-5096(63)90060-7

[49] Li Y, Wang W, Zhu B et al (2011) Elastic and thermodynamic properties of TiC from first-principles calculations.

Sci China Phys Mech Astron 54:2196–2201. https://doi.org/10.1007/s11433-011-4500-0

[50] Taya M, Hayashi S, Kobayashi AS, Yoon HS (1990) Toughening of a particulate-reinforced ceramic-matrix composite by thermal residual stress. J Am Ceram Soc 73:1382–1391

[51] Hsueh CH (2002) Modeling of elastic deformation of multilayers due to residual stresses and external bending. J Appl Phys 91:9652–9656. https://doi.org/10.1063/1.1478137

[52] Hsueh C-H, Becher PF (1996) Residual thermal stresses in ceramic composites. Part I: with ellipsoidal inclusions. Mater Sci Eng A 212:22–28

[53] Nisar A, Ariharan S, Venkateswaran T et al (2017) Effect of carbon nanotube on processing, microstructural, mechanical and ablation behavior of ZrB2-20SiC based ultra-high temperature ceramic composites. Carbon N Y 111:269–282. https://doi.org/10.1016/j.carbon.2016.10.002

[54] Watts J, Hilmas G, Fahrenholtz WG et al (2011) Measurement of thermal residual stresses in ZrB2-SiC composites. J Eur Ceram Soc 31:1811–1820. https://doi.org/10.1016/j.jeurceramsoc.2011.03.024

[55] Liu J, Vohra YK (1994) Raman modes of 6H polytype of silicon carbide to ultrahigh pressures: a comparison with silicon and diamond. Phys Rev Lett 72:4105–4108. https://doi.org/10.1103/PhysRevLett.72.4105

[56] Ghosh D, Subhash G, Orlovskaya N (2008) Measurement of scratch-induced residual stress within SiC grains in ZrB2–SiC composite using micro-Raman spectroscopy. Acta Mater 56:5345–5354. https://doi.org/10.1016/j.actamat.2008.07.031

[57] Watts J, Hilmas G, Fahrenholtz WG et al (2010) Stress measurements in ZrB2–SiC composites using Raman spectroscopy and neutron diffraction. J Eur Ceram Soc 30:2165–2171. https://doi.org/10.1016/j.jeurceramsoc.2010.02.014

[58] Nguyen VH, Shahedi Asl M, Delbari SA et al (2021) Effects of SiC on densification, microstructure and nano-indentation properties of ZrB2–BN composites. Ceram Int 47:9873–9880. https://doi.org/10.1016/j.ceramint.2020.12.129

[59] Debnath D, Chakraborty S, Mallick AR et al (2015) Mechanical, tribological and thermal properties of hot pressed ZrB2-SiC composite with SiC of different morphology. Adv Appl Ceram 114:45–54. https://doi.org/10.1179/1743676114Y.0000000189

[60] Sonber JK, Raju K, Murthy TSRC et al (2018) Friction and wear properties of zirconium diboride in sliding against WC ball. Int J Refract Met Hard Mater 76:41–48. https://doi.org/10.1016/j.ijrmhm.2018.05.009

[61] Nisar A, Khan MM, Bajpai S, Balani K (2019) Processing, microstructure and mechanical properties of HfB2-ZrB2-SiC composites: effect of B4C and carbon nanotube reinforcements. Int J Refract Met Hard Mater 81:111–118. https://doi.org/10.1016/j.ijrmhm.2019.02.014

[62] Savchenko N, Mirovoy Y, Burlachenko A et al (2021) Subsurface multilayer evolution of ZrB2–SiC ceramics in high-speed sliding and adhesion transfer conditions. Wear. https://doi.org/10.1016/j.wear.2021.203956

[63] Hassan R, Balani K (2020) Engineered role of SiC particle size on multi-length-scale wear damage of spark plasma sintered zirconium diboride. Adv Eng Mater 22:2000637

[64] Archard JF (1953) Contact and rubbing of flat surfaces. J Appl Phys 24:981–988

[65] Balani K, Harimkar SP, Keshri A et al (2008) Multiscale wear of plasma-sprayed carbon-nanotube-reinforced aluminum oxide nanocomposite coating. Acta Mater 56:5984–5994. https://doi.org/10.1016/j.actamat.2008.08.020